2019-06

STUDY OF WAVE-INDUCED LOAD EFFECTS ON A SUBMERGED BODY NEAR THE SURFACE

Suriben, Kristia

Monterey, CA; Naval Postgraduate School

NAVAL POSTGRADUATE SCHOOL

MONTEREY, CALIFORNIA

THESIS

STUDY OF WAVE-INDUCED LOAD EFFECTS ON A SUBMERGED BODY NEAR THE SURFACE

by

Kristia Suriben

June 2019

Thesis Advisor: Young W. Kwon
Co-Advisor: Joseph Klamo

THIS PAGE INTENTIONALLY LEFT BLANK

REPORT DOCUMENTATION PAGE	*Form Approved OMB No. 0704-0188*

1. AGENCY USE ONLY *(Leave blank)*	**2. REPORT DATE** June 2019	**3. REPORT TYPE AND DATES COVERED** Master's thesis

4. TITLE AND SUBTITLE STUDY OF WAVE-INDUCED LOAD EFFECTS ON A SUBMERGED BODY NEAR THE SURFACE	**5. FUNDING NUMBERS**
6. AUTHOR(S) Kristia Suriben	
7. PERFORMING ORGANIZATION NAME(S) AND ADDRESS(ES) Naval Postgraduate School Monterey, CA 93943-5000	**8. PERFORMING ORGANIZATION REPORT NUMBER**
9. SPONSORING / MONITORING AGENCY NAME(S) AND ADDRESS(ES) N/A	**10. SPONSORING / MONITORING AGENCY REPORT NUMBER**

11. SUPPLEMENTARY NOTES The views expressed in this thesis are those of the author and do not reflect the official policy or position of the Department of Defense or the U.S. Government.

12a. DISTRIBUTION / AVAILABILITY STATEMENT Approved for public release. Distribution is unlimited.	**12b. DISTRIBUTION CODE** A

13. ABSTRACT (maximum 200 words)

There is a growing interest in using unmanned underwater vehicles to perform a large array of tasks that require operation near the surface, and the wave-induced loads experienced by these vessels play an important role in their design and operation. An analytic solution can predict first-order loads on a submerged body using potential flow theory. However, potential flow does not take into account viscous effects, which can also be significant in the hydrodynamic loads experienced. Experimental model tests were performed using a wave generation tow tank, where both potential and viscous effects were acting on a submerged body, at speed, near the surface. Two different geometries were tested to model these submerged bodies. One model was a cylindrical body with hemispheric endcaps. The second model was a cylindrical body with circular, flat-faced endcaps. Experiments on both models were performed to measure hydrodynamic loads for three different speeds over various wavelengths, at two model depths, and for one wave height. The measured loads were then compared and analyzed against the predicted loads from the analytic solution, and the significance of viscous loads was determined.

14. SUBJECT TERMS unmanned, underwater, vehicle, hydrodynamic, forces, loads, waves, submerged, viscous, hemispheric, cylindrical, speed, tow, tank, potential, wavelength, model	**15. NUMBER OF PAGES** 95
	16. PRICE CODE

17. SECURITY CLASSIFICATION OF REPORT	**18. SECURITY CLASSIFICATION OF THIS PAGE**	**19. SECURITY CLASSIFICATION OF ABSTRACT**	**20. LIMITATION OF ABSTRACT**
Unclassified	Unclassified	Unclassified	UU

NSN 7540-01-280-5500 Standard Form 298 (Rev. 2-89) Prescribed by ANSI Std. 239-18

THIS PAGE INTENTIONALLY LEFT BLANK

Approved for public release. Distribution is unlimited.

STUDY OF WAVE-INDUCED LOAD EFFECTS ON A SUBMERGED BODY NEAR THE SURFACE

Kristia Suriben
Lieutenant, United States Navy
BS, U.S. Naval Academy, 2012

Submitted in partial fulfillment of the
requirements for the degree of

MASTER OF SCIENCE IN MECHANICAL ENGINEERING

from the

NAVAL POSTGRADUATE SCHOOL
June 2019

Approved by: Young W. Kwon
Advisor

Joseph Klamo
Co-Advisor

Garth V. Hobson
Chair, Department of Mechanical and Aerospace Engineering

THIS PAGE INTENTIONALLY LEFT BLANK

ABSTRACT

There is a growing interest in using unmanned underwater vehicles to perform a large array of tasks that require operation near the surface, and the wave-induced loads experienced by these vessels play an important role in their design and operation. An analytic solution can predict first-order loads on a submerged body using potential flow theory. However, potential flow does not take into account viscous effects, which can also be significant in the hydrodynamic loads experienced. Experimental model tests were performed using a wave generation tow tank, where both potential and viscous effects were acting on a submerged body, at speed, near the surface. Two different geometries were tested to model these submerged bodies. One model was a cylindrical body with hemispheric endcaps. The second model was a cylindrical body with circular, flat-faced endcaps. Experiments on both models were performed to measure hydrodynamic loads for three different speeds over various wavelengths, at two model depths, and for one wave height. The measured loads were then compared and analyzed against the predicted loads from the analytic solution, and the significance of viscous loads was determined.

THIS PAGE INTENTIONALLY LEFT BLANK

TABLE OF CONTENTS

LIST OF FIGURES

THIS PAGE INTENTIONALLY LEFT BLANK

LIST OF TABLES

THIS PAGE INTENTIONALLY LEFT BLANK

LIST OF ACRONYMS AND ABBREVIATIONS

cm	centimeters
ft.	feet
hz	hertz
in.	inches
m	meters
NPS	Naval Postgraduate School
RPM	revolutions per minute
sec	second
UUV	Unmanned Underwater Vehicle

THIS PAGE INTENTIONALLY LEFT BLANK

ACKNOWLEDGMENTS

I would like to thank Dr. Kwon and Dr. Klamo for their support and technical guidance throughout my course of work. I would also like to thank Mr. John Mobley, from the NPS machine shop, who helped me produce numerous structure pieces for this thesis.

THIS PAGE INTENTIONALLY LEFT BLANK

I. INTRODUCTION

The Navy needs unmanned underwater systems to engage in waters that traditional maritime platforms are denied from. Unmanned underwater vehicles (UUV) are considered to improve performance, reduce costs, and expedite tactical mission timeliness as the probability and extent of area denial grow with asymmetric threats.

The use of unmanned technologies is not a new concept, but efforts to continuously improve them to exploit vast oceans will influence the U.S. Navy's ability to successfully operate anywhere around the world. As naval forces move to and from the open ocean and littorals, challenging mission requirements will become increasingly hazardous for naval platforms and their crews. This has led to a growing interest in using UUVs to fill these gaps in capabilities. Many of their mission objectives would require the UUV to operate shallowly submerged, near the surface. This would expose the vehicle to wave-induced loads that must be addressed for efficient and effective operation. Sailors prepare to insert a UUV to search for underwater mines in Figure 1.

Figure 1. Sailors prepare to insert a UUV to search for underwater mines. Source: [1].

To address these wave-induced loads, it is preferred to use a closed-form analytic solution from linear inviscid flow theory to predict the first-order loads as this would allow the capability to make predictions quickly over a wide range of environmental and operating conditions. However, the validity of the results from potential theory in a real viscous flow environment is unknown. Loss of efficiency and ease is the result of computationally time-intensive methods of numeric simulations. The purpose of this thesis is to explore the extent to which viscous effects limit the accuracy of load predictions using potential flow solutions. Different speeds and geometry were imposed in this study to maximize the impact of viscous effects. Aside from the traditional hemispheric end cap, flat face end caps were also used. The flat face end cap should enhance the viscous effects by creating a flow separation. The measured loads are compared to the loads predicted from the closed-form analytic solution to determine the significance of viscous loads with respect to increased velocity and change in front face geometry.

A. PREVIOUS RESEARCH

For an inviscid fluid with a regular train of waves, the first order loads on a slender body of revolution can be solved analytically using the method of singularities. Cummins [2] derived the first-order net forces and moments for this case and conducted experiments to validate his theory. His results were notably scattered and were limited to the fact that the slenderness of the bodies must be large with ends that are not blunt. However, slenderness and bluntness qualities were not clear.

Khalil [3] conducted an experiment on the wave-induced forces acting on submerged horizontal cylinders. He showed that the magnitude of wave-induced forces on the submerged cylinders was dependent on depth, but he oriented the submerged bodies parallel to the incoming wave. His main conclusion was that the breaking of the waves in a shallow submerged case was responsible for the non-linear wave forces. His experiment studied cases at eight different depths but was limited to only one amplitude and two different wavelengths.

Ananthakrishnan and Zhang [4] studied how the dynamics of autonomous underwater vehicles (AUV) are affected when operating near the sea floor or surface

waves. They did this by creating a nonlinear hydrodynamic model and showed that the closer the AUV's proximity is to the sea floor or the surface waves, the stronger the hydrodynamic force it experiences.

Previous work by Turner et al. [5] and Jones et al. [6] conducted a similar model experiment. Turner et al. studied the potential and viscous effects of waves on a fully submerged vehicle of a specific canonical shape at zero speed, but operating near the surface. Jones et al. studied effects of a flat end face for a square cross section at zero speed. The two depths studied were at a nondimensional depth of 1.0 and 2.0. These experiments were performed on 4.5-inch diameter model over various wavelengths and for one wave height. Only hydrodynamic loads at zero speed were tested. He noted that for wave-induced drag, viscous effects are minor for zero speed and deduced that it would also be minor for cases with low forward velocity. Analytic solutions under predicted the vertical force and pitch moment for conditions when the wavelength is shorter than the body or if the body is shallow submerged. He hypothesizes that this was due to the change in wave height as the waves broke over the body. Analytic solutions were accurate for conditions with wavelengths longer than the body length, as long as it was at a sufficient depth. Figure 2 shows his graphical results.

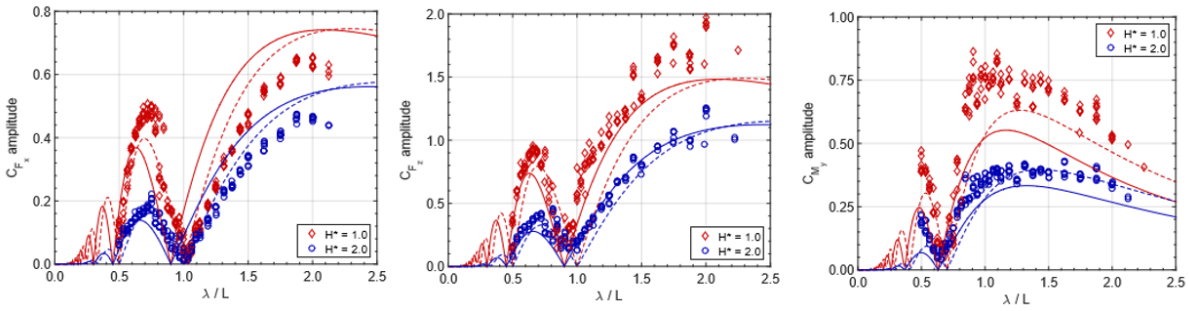

Figure 2. Experimental vs. theoretical results of non-dimensional drag force, vertical force, and pitch moment. Source:[5]

B. OBJECTIVE

This study will examine the accuracy of load prediction solutions obtained from inviscid potential flow for bodies with forward speed and separated flow over the body. The NPS tow tank provides the facility and capability to induce hydrodynamic loading on a submerged body and is capable of doing so at variable speeds. The two models used as the submerged bodies will be of different geometries. They will both have cylindrical parallel mid-bodies, but one will have hemispheric endcaps and the other will have flat-faced endcaps. Both models will be a length of 57.15 cm (22.5 in.) and have a diameter of 11.43 cm (4.5 in.)

The model will be tested at centerline depths of 11.43 and 22.86 cm (4.5 and 9 in.) which correspond to non-dimensional depths of 1 and 2 respectively. A single wave height of 5.08 cm (2 in.) will be used, and two speeds will be tested over a set of wave frequencies that span a wavelength to model length range of 1 to 4.125. The desired pitch and yaw angle for this study will be zero.

The hydrodynamic loads will be measured using a non-waterproof load cell, and the wave conditions and carriage speeds will be measured using position probes secured at appropriate locations. Wave profile, velocity profile, and load time history data will be recorded and used for analysis to compare against the predicted first order loads from the closed-form analytic solution from linear inviscid flow.

II. METHOD OF SOLUTION

A. THEORY

The general equations for the hydrodynamic forces for a slender body of revolution moving with a constant velocity subjected under a regular train of waves were derived by Cummins [2] in the early 1950s. Drag force, vertical force, and pitch moment are the equations used in this study and are expressed as equations 37, 39, and 57, respectively, in his report.

Cummins' equations involved integral expressions that take into account the geometry of the body which must be evaluated over its length. Turner et al. [5] simplified these equations by implementing a specific model geometry and that the incoming waves traveled along the longitudinal axis of the body. Equations 1 and 2 are the simplified drag and vertical forces where ρ is the fluid density, g is gravitational acceleration, A_o is the cross-sectional area of the body at the midpoint, h is the wave height, λ* is the nondimensional wavelength λ /L, H' is the nondimensional depth H/ λ , b_0 is an integral expression, ω_e is the encounter frequency, V is the model speed, c is the wave speed, and t is time. When comparing the two equations, the vertical force should be twice the magnitude and 90 degrees out of phase from drag force.

$$F_x = -\frac{\pi}{2} h(1/\lambda^*)(\rho g A_o) e^{-2\pi H'} b_0 \cos(\omega_e t) \tag{1}$$

$$F_z = -\pi h(1/\lambda^*)\rho g A_o (1 - \frac{V}{2c}) e^{-2\pi H'} b_0 \sin(\omega_e t) \tag{2}$$

$$M_y = \frac{\pi}{2} \rho g A_o h(1/\lambda^*) e^{-2\pi H'} ((1 - \frac{V}{2c}) a_{1+} (\frac{\lambda^* V}{2\pi c} b_0) \cos(\omega_e t) \tag{3}$$

Equation 3 is the pitch moment which contains additional terms, L, the length of the body and, a_1, an integral expression. The sign of a_1 and b_0 indicates whether the drag force and pitch moment lead or lag by 90-degrees, and the vertical force can be in phase or 180-degree out of phase.

Equations 1–3 are general because a_1 and b_o are geometry dependent integral expressions. Turner et al. evaluated these expressions for a circular cylinder with hemispheric end caps. There results can be found in [5] and will not be reproduced here. By taking only the middle portion of their integral expression results, the solution for a cylinder with flat end faces is obtained.

Using these equations, first-order drag force, vertical force, and pitch moment predictions were made for various speeds at a nondimensional depth of 1.0. These results are shown in Figures 3–5. The red data is for zero velocity, the green data is for a velocity of 0.381 m/sec (1.25 ft./sec), the blue data is for velocity of 0.762 m/sec (2.5 ft./sec), and the black data is for a velocity of -0.762 m/sec (-2.5 ft./sec). Positive velocities indicate head seas and negative velocities indicate following seas. Based on theoretical predictions, drag force is expected to remain unchanged when speed is applied to the model. Additionally, vertical force is expected to increase with speed, and pitch moment peak magnitudes are expected to increase with speed.

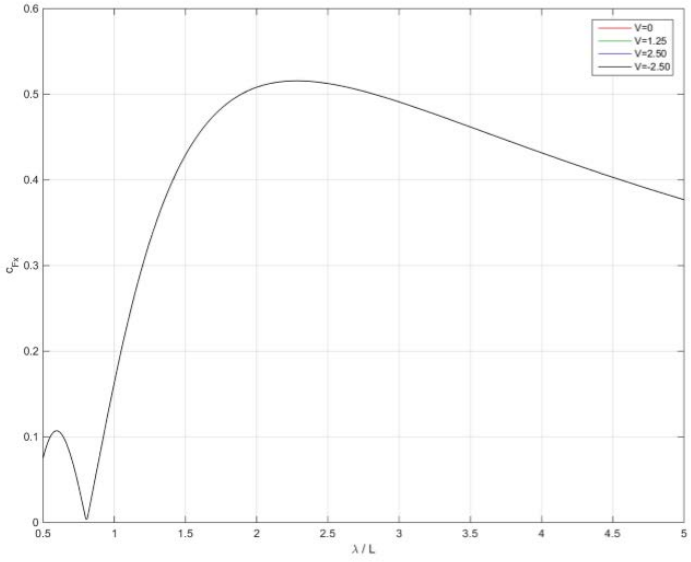

Figure 3. First-order oscillating drag force predictions from Cummins' theory

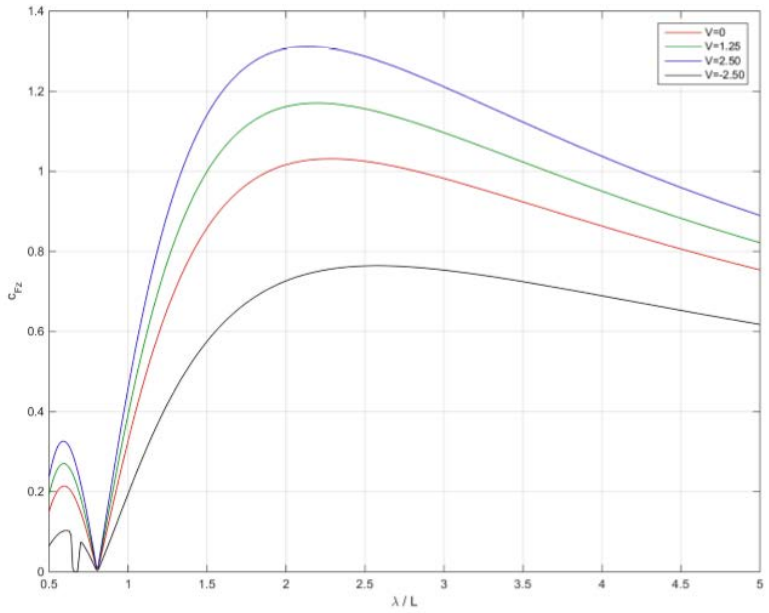

Figure 4. First-order oscillating vertical force predictions from Cummins' theory

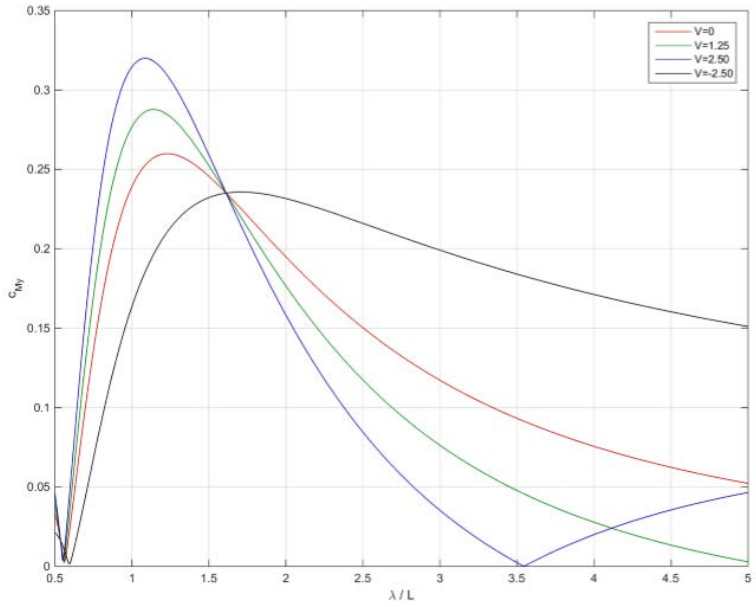

Figure 5. First-order oscillating pitch moment predictions from Cummins' theory

B. EXPERIMENTAL SETUP

1. Tow Tank and Wavemaker

Tests were conducted in the wave tow tank in the Hydrodynamics Laboratory at the Naval Postgraduate School. The aluminum tow tank is 0.914 m (3 ft.) wide by 1.219 m (4 ft.) deep and 10.97 m (36 ft.) long. Plexiglas panels were used to allow for visual observation of waves and models underwater during testing [5]. Additionally, there is an aluminum tow carriage that runs the length of the tank on two rails that are mounted on top of the sides of tank and run parallel to each other. Figure 6 shows the tow tank and its overall dimensions.

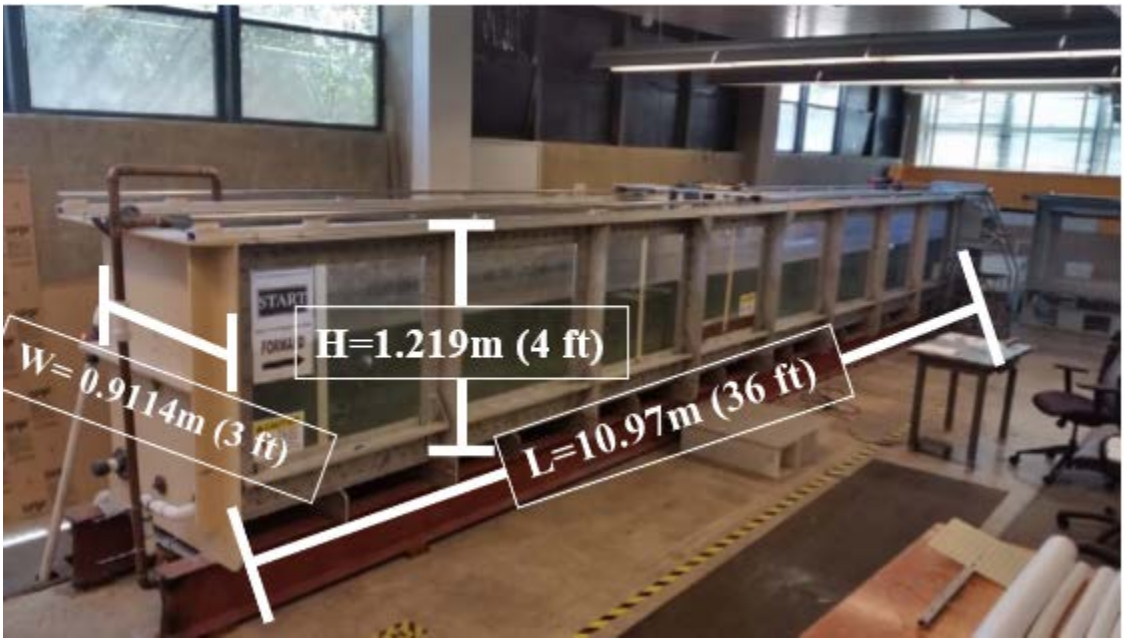

Figure 6. Tow tank dimensions. Source: [7].

The wavemaker is a wedge that moves vertically in an oscillating motion. It is driven by a MOOG Animatics MT electric motor (SM34165MT), a Modusystems Pulse/Dir motor controller (MAC-2TC), and an E-Drive L-TAC LS long stroke ball screw linear actuator (LS204-24). The wedge is 0.609 m (2 ft.) deep and fits within the width of the tank. One side of the wedge is at 35-degree angle from the other side that is vertical. The wave wedge geometry is shown in Figure 7. At the opposite end of the tank is a wave beach that dissipates

the waves and minimizes its reflection. The two staggered layers are perforated acrylic sheets that span the width of the tank and are 121.92 cm (48 in.) in length. This is shown in Figure 8. The two sheets are fixed at an inclined angle of about 12 degrees [5].

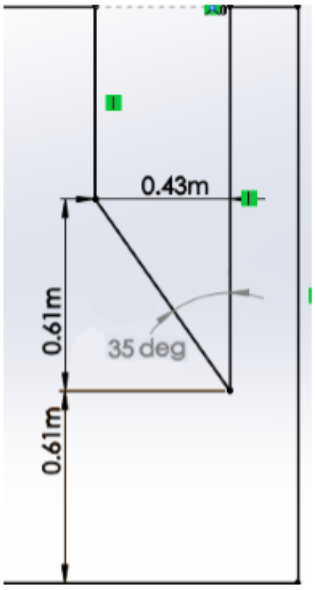

Figure 7. Wavemaker wedge geometry. Source [8]

Figure 8. Beach made out of perforated acrylic sheets

2. Model and Fixture

Both models used for testing were hollow with a 11.43 cm (4.5 in.) diameter circular cylindrical body and a total length of 57.15 cm (22.5 in). Two different geometric faces were used. The first geometry tested had hemispheric end caps on each end. The second geometry tested had flat-faced circular end caps at each end. The model body and end caps were made from polycarbonate material using the rapid prototyping feature on a Fortus 400mc 3D printer. Another surface feature implemented from Turner et al. study were a series of bleed holes on the model to ensure it was free-flooding and that all the air was pushed out of the body after it was submerged. Figure 9 shows the model geometries with a measuring tape extended out to 30.48 cm (12 in.) for spatial reference.

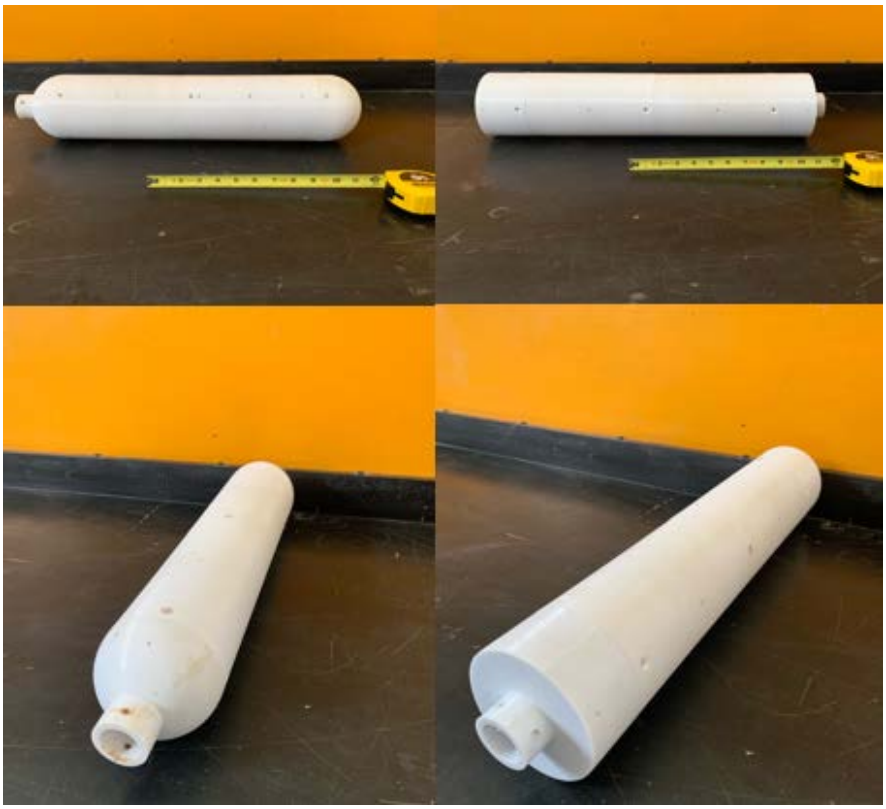

Figure 9. Model with hemispheric end caps and model with flat face end caps

The model was attached to the carriage assembly using a test structure that was able to support a sting fixed to it. Figure 9 shows the model attached. The sting passed through the stern of the model and extended inside the model. At the midpoint inside the model is a circular collar to provide more rigidity to the structure. The vertical part of the sting is a 3.81 by 2.54 cm (1.5 by 1.0 in.) aluminum bar that was 105.41 cm (41. 5 in.) long. Holes were drilled every 2.54 cm (1 in.) to allow easy depth adjustments of the model [5]. The vertical part of the sting was attached to a U-shaped channel that was also made of aluminum which was directly fixed to the load cell. The load cell was bolted to the carriage via an aluminum block that converted the bolt holes of the load cell to the bolt holes of the carriage. The load cell was not located on the model and instead, above the model. Because of this, the difference in position between the load cell and model must be known to move the pitch moment from the load cell origin to the model origin where the forces and moments are reported from. Figure 10 shows how the sting, U-channel, and model were configured.

Figure 10. Sting style text fixture with model attached. Source: [5].

To mitigate the drag force and wake formed from of the rectangular cross section of the sting, a fairing was produced also using the rapid prototyping on the Fortus 400mc

3D printer and made of polycarbonate. This fairing wrapped around the sting bar and extended from the depth of the model. It is symmetric for to aft with a chord of 26.67 cm (10.5 in.), thickness of 5.08 cm (2 in.), and span of 24.76 cm (9.75 in.). The fairing was fixed to the sting bar, aligned to the longitudinal axis of the model, and was not free to rotate. Figure 11 shows how the fairing integrated with the model fixture.

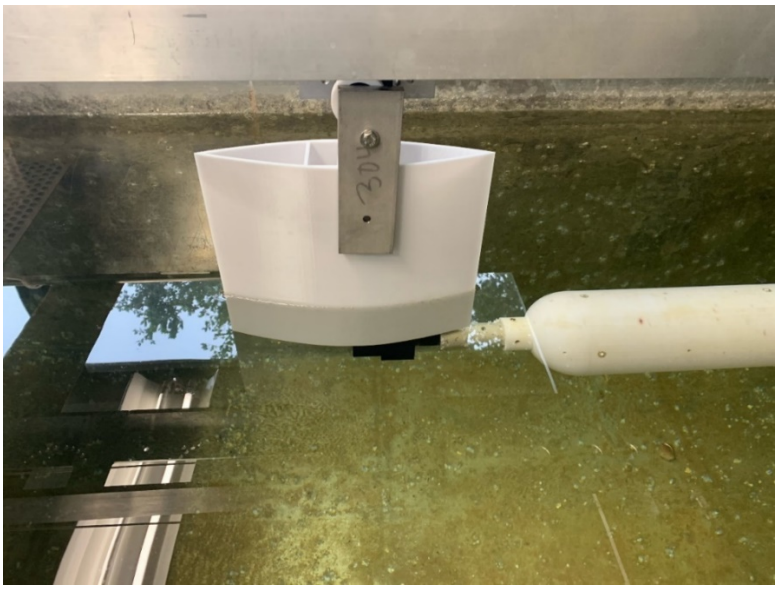

Figure 11. Fairing installed around sting

3. Carriage Pulley Assembly

A Baldor Super-S motor was used to drive the carriage assembly through the water using a pulley system. It is a 5 horse-power at 230V, 60 Hz AC power motor with a maximum speed of 1750 RPM [9]. The motor controller is the Baldor VS1SP AC inverter where the desired voltage and Hz are used as inputs in numerous modes of operations. For this experiment, the controller was only used in Profile Setting. This allowed the user to input the desired speed in the form of Hz and desired acceleration and deceleration time in seconds. The speed of the motor is controlled by an input frequency which is supplied to the motor. The minimum speed setting available is 2.5 Hz while the maximum available is 30 Hz [9], and due to the limited length of the tow tank, it was unsafe to operate at a speed exceeding 4.5 Hz.

The carriage platform runs the length of the tank on a pair of parallel rails mounted to the top of the tank. The platform is an aluminum plate 1.905 cm (0.75 in.) thick with 5.08 cm (2 in.) spaced holes to allow for an easy way to secure instruments and sensors. The carriage configuration for these experiments had, as mentioned, the model attached via the sting style fixture. In addition, an 80/20 aluminum bar extended in front of the carriage to hold two ultrasonic probes that measured wave height. It also held a Plexiglas panel flat surface which reflected the ultrasonic pulses from a position probe that measured the carriage position.

Since the carriage platform was only held to the tank at the two end and is quite thin, it was subject to bending and vibrations during carriage movement. These carriage vibrations caused excess noise in the various sensors that were attached to the carriage. Two 80/20 aluminum bars were installed to the top of the carriage and pinned down at points along the width to reduce the impact of bending and vibrations on the measurements. Figure 12 shows the strengthening beams on the carriage platform.

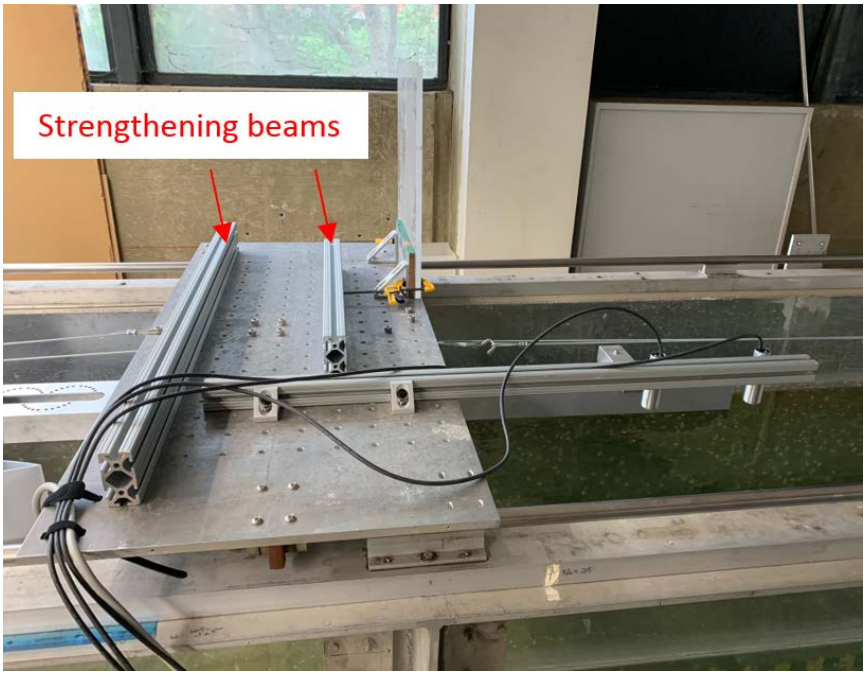

Figure 12. 80/20 aluminum beams pinned to reduce noise and vibration in the carriage

4. Carriage Speed Calibration

The carriage speed with the new pulley assembly had to be calibrated against the motor. This was done visually over a known distance with a stop watch. Multiple runs were conducted at different motor inputs starting at 2.5 Hz up to 3.5 Hz. At a 2.5 Hz input, an output carriage speed of about 0.381 m/sec (1.25 ft./sec) was observed. As the motor input was increased, the carriage speed was observed to increase linearly. Figure 13 shows the linear relationship between the motor input and carriage speed output. Equation 4 was the linear curve fit equation used.

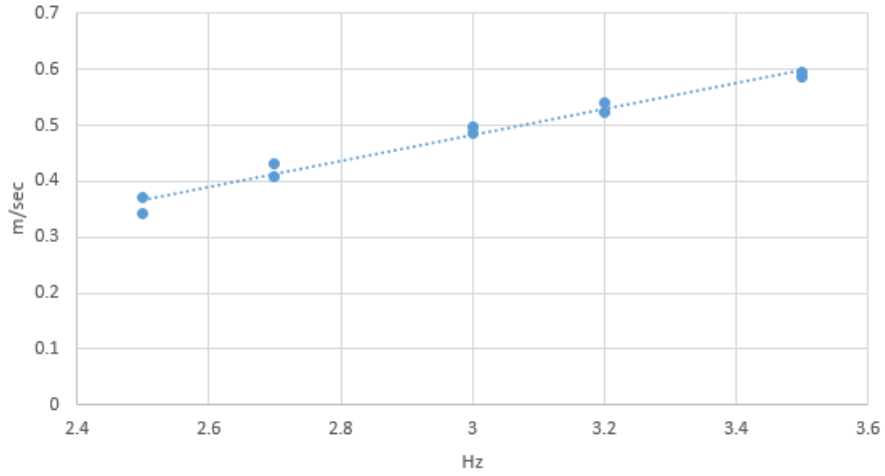

Figure 13. Motor input and carriage speed output

$$\text{speed (m/sec)} = 0.1615\ \text{MotorHz} + 0.8902\text{(m/sec)} \qquad (4)$$

5. Carriage Setup Verification

In order to expand the previous work in the lab by Turner et al., the results needed to be duplicated using the new test set-up mounted to the carriage instead of the fixed bridge. Figures 14 and 15 show previous vertical force measurements against the new vertical force measurements taken from the new carriage assembly for zero speed cases. The loads measured from the carriage assembly virtually matched the loads measured from the previous stationary bridge assembly for a nondimensional depth of 1.0. A slight

difference of 0.1 lbs between the data is apparent at a nondimensional depth of 2.0 which was deemed acceptable. The replication of the stationary data allowed the use of the bridge assembly data reduction process on the new carriage pulley assembly setup.

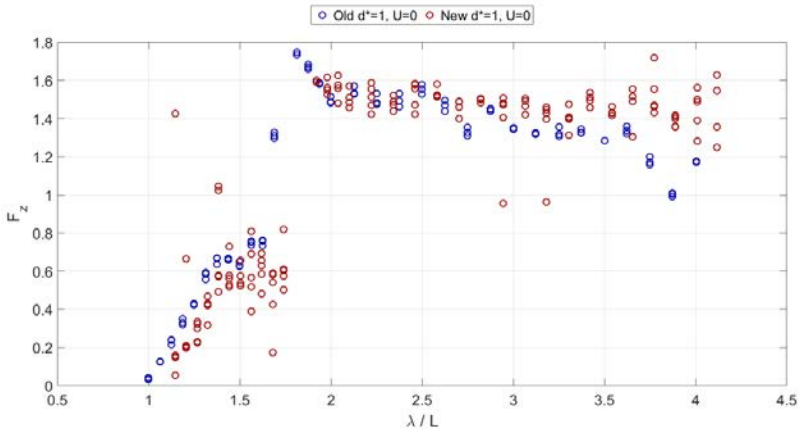

Figure 14. Vertical force measurement at zero speed taken at various frequencies at a nondimensional depth of 1.0

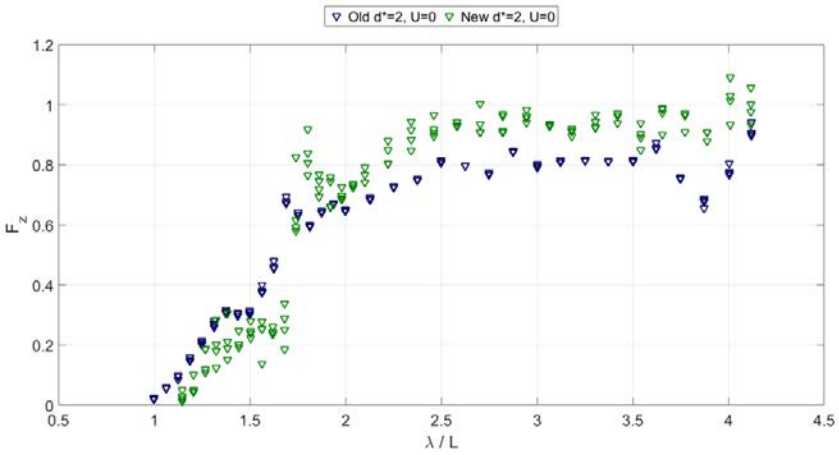

Figure 15. Vertical force measurement at zero speed taken at various frequencies at a nondimensional depth of 2.0

Additionally, the ultrasonic probe used to measure carriage position was new to the setup and tests were conducted to verify the manufacturer's calibration. The ultrasonic probes used for wave height's calibration was already verified by Whitmer [10] in a

previous experiment that utilized the NPS wave generation tow tank. The carriage position probe was set to measure distances between 76.2 and 838.2 cm (30 and 330 in.). A Plexiglas plate was fixed to the top of the carriage to give the ultrasonic probe a flat surface to reflect off of. The Plexiglas configuration is shown in Figure 17. Known distances from the probe were marked and the carriage was moved to each position to verify the probe readings. Next, carriage runs were conducted to track the movement of the carriage. Position versus time data was collected and velocities were calculated and compared to the visual carriage speed calibration conducted in Section II.B.4. Figure 16 shows the distance versus time plot for an input of 4.5 Hz and an output speed of about 0.762 m/sec (2.5 ft./sec). The velocity calculated using the ultrasonic probe agreed with the velocity calculated in section II.B.4.

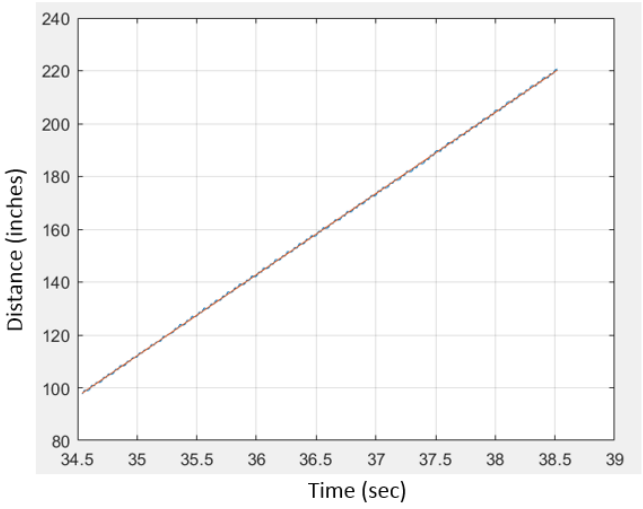

Figure 16. Ultrasonic probe measurements used to calculate the velocity

6. Instrumentation

The hydrodynamic forces acting on the model were measured using a non-waterproof AMTI MC3A load cell. The sensor measures force and moment components in three dimensions, producing a total of six outputs. Each channel could be set for a specific excitation voltage [11]. Since different model depths required different measurement range requirements, each channel was set to the optimized resolution and signal to noise ratio for

that depth. The load cell was connected to an AMTI Gen5 amplifier and a signal conditioner. This compensated for the effects of the cable length for the analog output voltage and allowed for specific channel settings. Table 1 shows the measurement range used for the two depths used.

Table 1. Load cell measurement range for two model depths tested. Source: [5].

H^* (–)	F_x (N)	F_z (N)	M_y (N-m)
1	±92.03	±362.57	±13.35
2	±92.03	±362.57	±26.60

Four Senix ToughSonic 14 ultrasonic probes were used to measure distance and determined the wedge motion and wave height. The probe used to determine wedge motion was mounted above a horizontal member of the wedge support frame which oscillated with the wedge. The three probes that were used to measure wave height were mounted to the carriage assembly. Two of the probes were positioned to measure wave height approximately 50.8 cm (20 in.) in front of the model with 20.32 cm (8 in.) spacing between them to measure incoming wave profile. The remaining probe was positioned over the model, 15.24 cm (6 in.) forward of the model midpoint, which allowed for the measurement of any changes in wave height due to interaction with the model.

One Senix ToughSonic 30 ultrasonic probe was attached to one end of the tank and measured carriage distance. The difference in this specific probe is the optimum and maximum range specifications. The maximum range for the Senix ToughSonic 14 was 4.26 m (14 ft.) while the maximum range for the Senix ToughSonic 30 was 9.14 m (30 ft.) which allowed for position measurements for the length of the carriage [12]. A Plexiglas

plate was installed to the top of the carriage platform to give the ultrasonic probe a distinct flat surface to reflect off of. This layout is shown in Figure 17.

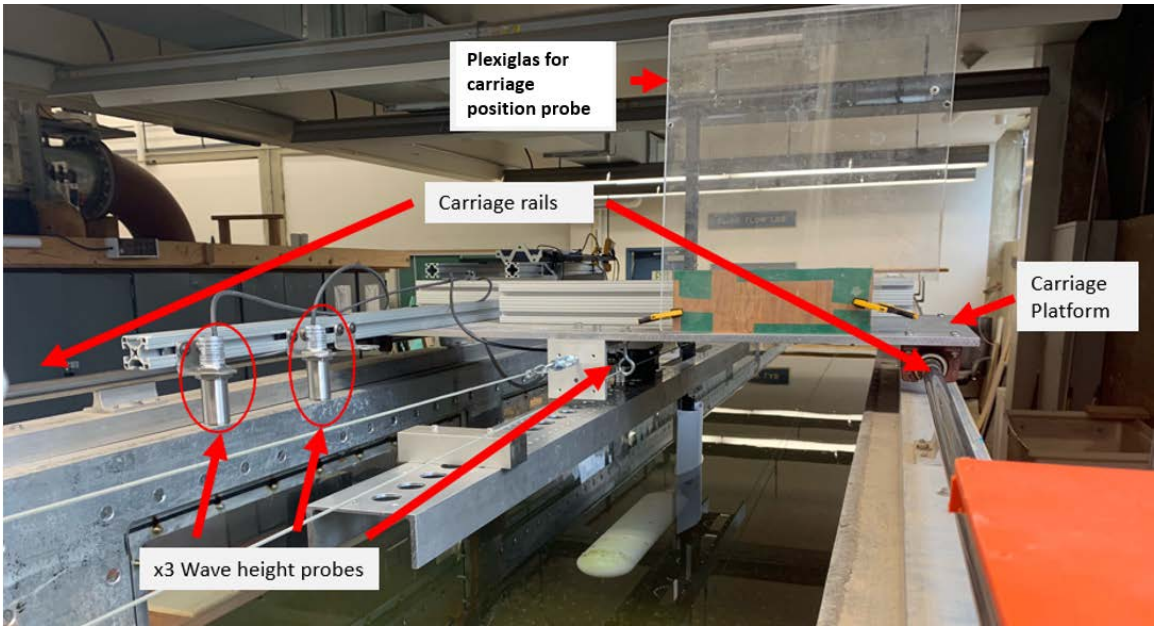

Figure 17. Carriage setup

The data was collected on a laptop computer (Dell Precision 17 7000 series) using MATLAB's data acquisition toolbox function and a custom-written script. Analog voltages from the sensors were channeled into a DAQ board: NI USB-6363 X Series DAQ Device with BNC termination.

7. Wavemaker Structural Strengthening

The wavemaker is a wedge that moves vertically in an oscillating motion. When the wedge is driven down, it pushes the water at the face of the wedge down the length of the tank and creates the wave. The force that the wedge face exerts on the water in the direction of the length of the tank is translated back to the wedge in the opposite direction, in equal magnitude. This, coupled with the lack of rigidity in the roller bearing, resulted in excessive motion in the wedge structure which often caused the actuator to fault and cease wedge movement.

To combat this excessive motion, the original setup had two support members, running horizontally, secured between the wedge and the top of the support fixture. This was intended to resist movement in the horizontal direction, but allowed free movement in the vertical direction using two rollers which straddled the vertical support members of the wedge. Figure 18 shows this setup. This proved to be sufficient for a set of uniform waves, but in cases where irregular waves were desired, the change in amplitude and frequency of the wedge motion between two different wave profiles caused even more force and movement in the horizontal direction. The rollers did not prove to be robust enough. It was not close-fitting to the vertical members. Additionally, the way the rollers were pinned to the horizontal members in order to allow for rotational motion made it unstable against the translated horizontal force from the wedge. Because of this, the wedge actuator often would fault and cease movement for irregular wave settings.

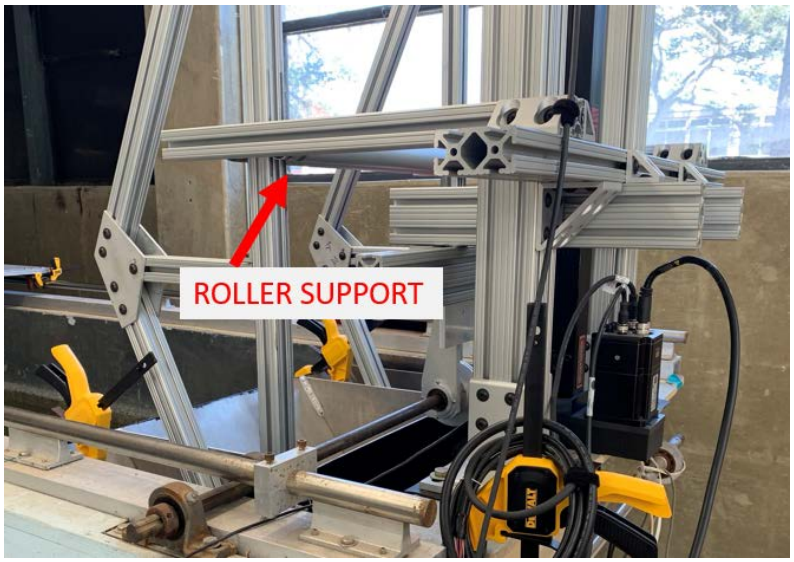

Figure 18. Wedge support structure with previous roller support installed

The next, and current, iteration to this structure was to replace the rollers with Teflon sleeves. The Teflon sleeves closely hugged the vertical support members and allowed motion in the vertical direction. Instead of being pinned, it was now securely fixed to the horizontal support member with an additional diagonal support member to resist the

effects of the moment arm. This proved to be robust enough to resist the force translated in the horizontal direction. Figure 19 shows the current wedge structure.

Figure 19. Current wedge support structure with Teflon sleeves

C. EXPERIMENTAL PROCEDURE

Each test condition was carried out in the following procedure: The wave maker was set to the desired frequency and amplitude and started. Once the first few waves had propagated down the tank and past the model, the data collection process was started which collected at 50 Hz for a total of 60 seconds. The first 30 seconds of data were used collecting data for the carriage at zero speed. This data was used to further validate previous data for forces and moments on the model at zero speed by Turner et al. After the first 30 seconds, the carriage run profile was started at the desired speed input frequency. The carriage would accelerate to the desired speed and would have to be stopped manually with the remote controller before the end of the tow tank. These 30 seconds of data would be used for the at-speed analysis. The data collected would be written as an ASCII time history file for data reduction later. The wave frequencies were tested at a random order and each

frequency was tested two times for a given speed to in order to assess the amount of uncertainty in the data points.

The two depths used for this study were at 11.43 and 22.86 cm (4.5 and 9 in.) from the center of the model. These depths corresponded to a non-dimensional depth of 1 and 2 respectively. A single wave height of 5.08 cm (2 in.) was used throughout the study. Runs were conducted at speeds 0.381, 0.762, and -0.762 m/sec (1.25, 2.5 and -2.5 ft./sec) with the waves approaching along the longitudinal axis of the model. Each speed setting was tested over thirty-three different wave frequencies that ranged from 0.816 to 1.716 Hz that spanned a wavelength to model length range of 1 to 4.125. The desired pitch and yaw angles of the model were both zero.

THIS PAGE INTENTIONALLY LEFT BLANK

III. DATA COLLECTION AND REDUCTION

A. DATA REDUCTION

The data from the ultrasonic probes and load cell was collected by the data acquisition board and stored to a computer. Data reduction was performed using a custom-written Matlab script. There were 11 channels used for data collection and that displayed their measurements in real-time. Channel 1 displayed the ultrasonic probe that measured wedge position. Channels 2 and 3 displayed the probes that measured the height of the incoming wave. Channel 4 showed the measured wave height over the model. Channel 5 showed the measured carriage position. Finally, channels 6–11 displayed the load cell measurements for the force and moments. All raw data collected was saved onto .dat files which would be used in the data reduction.

A zero file was collected at the beginning of each testing session to establish the nominal readings from each sensor. The nominal readings from the initial zero file were removed from the time histories of each collected channel for each run. The gain for each sensor was applied to each channel to convert the sensor output voltage readings to physical units. The hydrodynamic loads measured and displayed through channels 6–11 were then multiplied by an orientation matrix to convert the coordinate system from the sensor orientation to the model orientation. The model coordinate system's origin was chosen to be at the center of buoyancy of the model. Positive X-axis is towards the bow, positive Y-axis is towards the port side of the model, and positive Z-axis is up.

The next step in data reduction was to take the probe measurements for each run and interpret the sinusoidal wave signal to solve for wave amplitude and phase. Equation 4 is the least squares curve fit of the wave elevation from each probe used in the custom MATLAB script to determine amplitude and phase of a set of waves for the selected .dat file.

$$f_1(x,t) = A_1 \cos(kx - \omega_e t) + B_{1,} \sin(kx - \omega_e t) + C \tag{4}$$

$A_{1,}$ and $B_{1,}$ are the cosine and sine components of the first order amplitude, k is the wave number $2\pi/\lambda$, x is the probe location, ω_e is the wave encounter frequency and C is the wave elevation offset. Trigonometric identities can be used to simplify to a single first-order wave amplitude, a_w, and we are able to solve for the phase angle, $\varphi_{w,}$ relative to a sine wave. Since the probes were all at different locations, a spatial term in Equation 4 is necessary in order to have the phase referenced from a common point. The phase angle of each wave component was determined to be the average of the phases from the two probes located ahead of the model.

For cases where the model is stationary, the frequency at which the model encounters the incoming wave is simply equal to the frequency of the wave. For cases where the model is traveling at a certain velocity, the encounter frequency is impacted by both the frequency of the approaching wave and the wave's relative velocity to the model.

To determine the encounter frequency, the discrete fast Fourier transform was applied to the load history data from the load cell. The frequency component with the maximum energy obtained from the complex oscillating load data was determined to be the encounter frequency. The encounter frequency can be determined by applying the discrete fast Fourier transform to any of the load history data or to the wave history data from the ultrasonic probes. The encounter frequency obtained from the pitch moment load history was used as the common encounter frequency across all calculations because it had the largest signal magnitude.

Equation 5 is the finite depth third-order dispersion relationship that was used to estimate the wavelength. Here, g is the gravitational acceleration, k is the wave number, a is the first-order wave amplitude, and ω_i is the wave frequency.

$$\omega^2 = (gk\sigma)\{1+\frac{9-10\sigma^2+9\sigma^4}{8\sigma^4}(ka)^2\}+o((ka)^4) \tag{5}$$

$$\sigma = \tanh kh \tag{6}$$

It is also important to note that the measured drag force and pitch moment from the load cell also includes the effects of the sting and the drag induced pitch moment that

resulted from the difference in location between the load cell and the model. To match the theoretical model, these load contributions had to be removed from the load cell measurements. Doing this would reveal the loads experienced on the model only due to its interaction with the wave dynamics.

To remove the sting effects from the measured forces and moments at the load cell, testing was conducted only on the sting, mirroring the test conditions of the runs with the models rigged. Using the same custom MatLab script used for data reduction for test runs with the model, we were able to capture the cosine and sine components of the first-order amplitude and the phase shift of the loads and waves for the data with only the sting rigged. Equations 7 and 8 are the corrected, model only, drag and vertical force time histories where $F_{x,L}(t)$ and $F_{z,L}(t)$ are the load cell's as-measured drag and vertical force, $a_{Fx,S,}$ and $a_{Fz,S}$ are the drag and vertical force amplitudes of the sting, ω_e, is the encounter frequency, $\varphi_{Fx,S,w}$ and $\varphi_{Fz,S,w}$ are the drag and vertical force phase of the sting, and $\varphi_{w,}$ is the phase of the incoming wave.

$$F_{x,M}(t) = F_{x,L}(t) - a_{Fx,S}\sin(-\omega_e t + \varphi_{Fx,S\,|\,w} + \varphi_w) \tag{7}$$

$$F_{z,M}(t) = F_{z,L}(t) - a_{Fz,S}\sin(-\omega_e t + \varphi_{Fz,S\,|\,w} + \varphi_w) \tag{8}$$

To correct the pitch moment, the sting effects as well as the pitch moment due to the model drag needed to be removed. Equation 9 takes care of both corrections. It moves the pitch moment to the model origin and subtracts the sting effects. $M_{y,L}(t)$ is the load cell as-measured pitch moment, $a_{My,S}$ is pitch moment amplitude from the sting, $\phi_{My,S\,|\,w}$ is the sting only phase, ℓ is the vertical distance between the load cell and model origin, and $a_{Fx,M}$ and $\phi_{Fx,M\,|\,w}$ is the amplitude and phase angle of the model only drag force.

$$\begin{aligned} M_{y,M}(t) &= M_{y,L}(t) - (a_{My,S}\sin(-\omega_e t + \varphi_{My,S\,|\,w} + \varphi_w)) \\ &-\ell(a_{Fx,M}\sin(-\omega_e t + \varphi_{Fx,M\,|\,w} + \varphi_w)) \end{aligned} \tag{9}$$

After removing the effects of the sting, the resultant forces and moments on the model were still complex oscillatory signals. The load amplitude and phase of these load signals were calculated in a similar manner to what was done for the wave amplitude and

phase. Equation 10 is the least-squares curve fit equation for load amplitude and phase. A_2 and B_2 are the cosine and sine component of the nonlinear amplitude. This equation does not need a spatial term since the load cell is located at the model origin. The cosine and sine components were combined into the model force and moment amplitudes and phase angles relative to the sine wave.

$$f_2(0,t) = (A_1\cos(-\omega_e t) + B_1\sin(-\omega_e t)) + (A_2\cos(-2\omega_e t) + B_2\sin(-2\omega_e t)) + C \tag{10}$$

To properly carry out these set of calculations, the sting-corrected drag and vertical force from Equation 7 and 8 needed to be solved before determining the amplitude and phase of the model drag and vertical force using Equation 10. Only after that are we able to utilize Equation 9 to find the time history correction for the sting effects. Then again, use Equation 10 to determine the corrected amplitude and phase of the model pitch moment.

B. STEADY STATE DETERMINATION

Carriage position, drag force, and pitch moment time histories were analyzed alongside each other in order to determine when the system reached steady state. Steady state was assumed to be when carriage position versus time was linear and when the drag force and pitch moment versus time oscillated at a relatively constant amplitude and frequency. As stated in Section II.C, each run began with 30 seconds of data collection at zero speed, then the carriage run profile was started, and data was collected with the carriage moving. During the data cleaning, four indices during the run time had to be determined to be used for data analysis. Index one was where the time of carriage motion started. Index two was the time estimated, by visually inspecting all three time histories, where steady state started. Index three was the time steady state ended, right before stopping the carriage run profile. Index four was the time the carriage came to a complete stop. This process was done for each run. An example of the indices chosen for a given run is shown in Figure 20.

In the data analysis, data until Index one was analyzed as a zero velocity case. Data between indices two and three were assumed to be when the system was at steady state and would be analyzed as cases with forward speed.

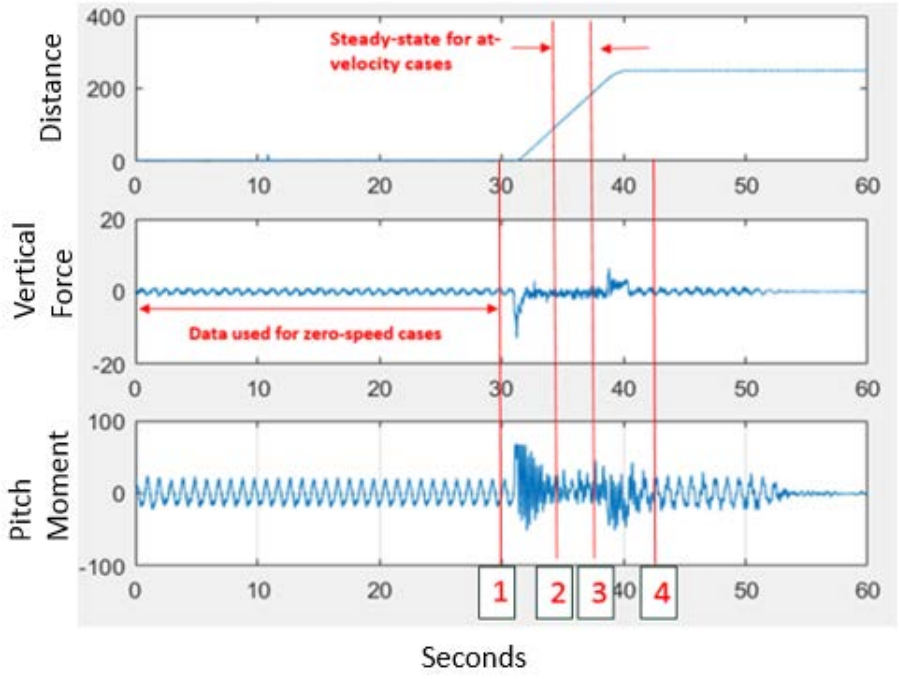

Figure 20. Determined zero speed and steady-state time for a given run

C. TEST MATRIX

A test matrix was used to systematically execute the complex variations of wedge frequency, amplitude, and model depth. It incorporated the variations in model speed and geometry for this study. The test matrix takes inputs like desired wave height, model length, wavelength, and water depth, applies a transfer function, and outputs the command frequency and amplitude of the wedge for each desired wave frequency. Figure 21 is an example of part of a test matrix. Desired λ/L ranged from 1.000 to 4.125 for each combination of model geometry, depth, and speed.

water depth =		3.000 (ft)		0.914 (m)			
max wave lenth =		6.000 (ft)		1.829 (m)			-0.225
Desired Wave Height =		2.000 (inches)		0.051 (m)			1.562
model length =		22.500 (inches)		0.572 (m)			-0.526
	desired	required	required				ITERATED
	lambda / L	wave length	wave length	steepness	period	freq	wedge CMD
	(---)	(ft)	(m)	(---)	(sec)	(Hz)	(mm)
1.000	1.000	1.875	0.572	11.250	0.583	1.716	36.571
2.000	1.063	1.992	0.607	11.953	0.603	1.658	37.670
3.000	1.125	2.109	0.643	12.656	0.623	1.605	38.756
4.000	1.188	2.227	0.679	13.359	0.642	1.558	39.830
5.000	1.250	2.344	0.714	14.063	0.660	1.515	40.893
6.000	1.313	2.461	0.750	14.766	0.678	1.475	41.947
7.000	1.375	2.578	0.786	15.469	0.695	1.438	42.991
8.000	1.438	2.695	0.822	16.172	0.712	1.404	44.028
9.000	1.500	2.813	0.857	16.875	0.729	1.373	45.057
10.000	1.563	2.930	0.893	17.578	0.745	1.343	46.081
11.000	1.625	3.047	0.929	18.281	0.760	1.315	47.098
12.000	1.688	3.164	0.964	18.984	0.776	1.289	48.111
13.000	1.750	3.281	1.000	19.688	0.790	1.265	49.119
14.000	1.813	3.398	1.036	20.391	0.805	1.242	50.124
15.000	1.875	3.516	1.072	21.094	0.820	1.220	51.125
16.000	1.938	3.633	1.107	21.797	0.834	1.200	52.123

Figure 21. Test matrix example

IV. DATA RESULTS

A. HEMISPHERICAL GEOMETRY

1. Comparison of Oscillating Load Amplitudes Due to Speed and Depth

Figures 22 and 23 show the amplitude of the oscillating drag force component at the encounter frequency for the model with hemispheric end caps at different speeds at a nondimensional depth of 1.0 and 2.0 respectively. The red data is for zero velocity runs, the blue data is for a velocity of 0.381 m/sec (1.25 ft./sec), the green data is for velocity of 0.762 m/sec (2.5 ft./sec), and the yellow data is for a velocity of -0.762 m/ sec (-2.5 ft./sec). Positive velocities correspond to head seas and negative velocities correspond to following seas. The black dash line is the theoretical prediction for drag force which, for a symmetric body in an inviscid fluid, has no dependence on forward speed. The data for zero speed cases are well grouped together which gives a higher confidence of its accuracy. It also appears that the quality of the data decreases with speed, which makes drag force unclear for at-speed cases, but it is evident that there are trends with respect to speed. Although the drag force values do not match theoretical results, the behavior between the theoretical results and actual results are similar. The results show that the drag force across all speeds shift to a lower magnitude when placed at a lower depth, which agrees with the theory.

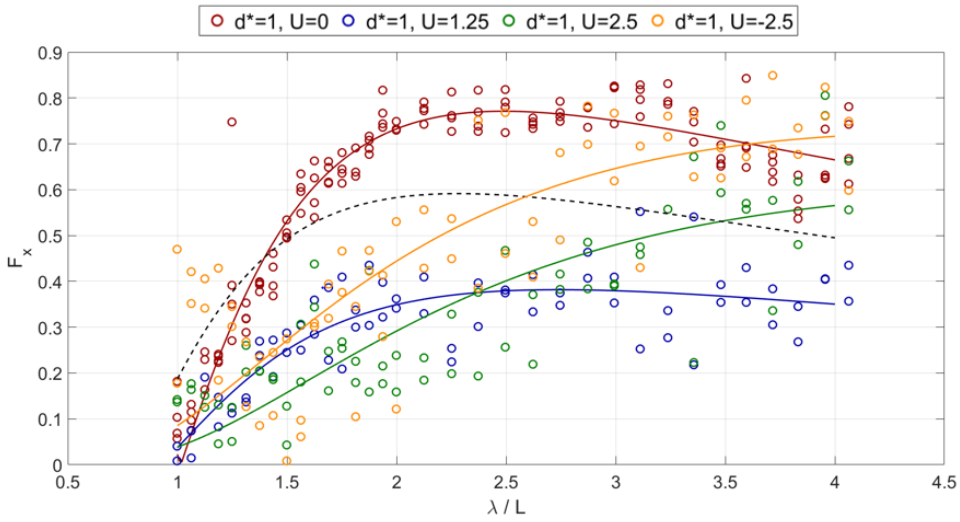

Figure 22. Drag force results for model with hemispheric end caps at a nondimensional depth of 1.0

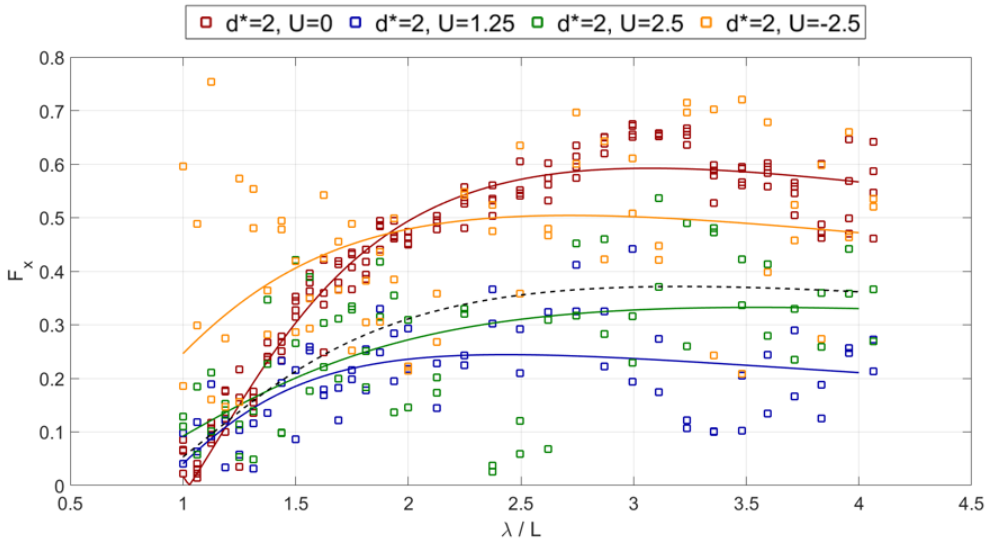

Figure 23. Drag force results for model with hemispheric end caps at a nondimensional depth of 2.0

It is interesting to note that at a nondimensional depth of 1.0, drag force decreases when the model is traveling at speed since theory shows speed has no impact on drag force. It is not clear if there is a relationship between the specific velocity and the amount of

decreased drag force due to the overlap in data for different speeds and, again, the scatter. The decrease in drag force for nondimensional depth of 2.0 is also noticeable for forward velocity cases. There were no distinct trends noted in cases with negative velocity.

Also notable is that Cummins' theory only considers inviscid flow and its effects while this experiment contained viscous effects. The drag force for forward velocity cases contain both the oscillating drag force only due to wave-induced drag and the steady mean drag force induced from the model moving in a viscous fluid. Yet, the data shows that the theoretical results over predict the oscillating drag force for cases with forward speed over the whole testing frequency spectrum.

Figures 24 and 25 show the vertical force with the model at different speeds at a nondimensional depth of 1.0 and 2.0 respectively. The color formatting is the same as Figure 19, and theoretical results are displayed as dashed lines with their colors corresponding to their appropriate speeds. Vertical force has a larger signal to noise ratio than drag force and thus less scatter. When increasing the model velocity to 0.381 m/sec (1.25 ft./sec), it does not appear that the vertical force is impacted. However, for a velocity of 0.762 m/sec (2.5 ft./sec), there is a slight, but clear, increase in vertical force across the frequency spectrum tested. Additionally, for cases with velocity at -0.762 m/sec (-2.5ft./sec), there is a sufficient decrease in vertical force. When comparing different depths, the model experiences more vertical force for a nondimensional depth of 1.0 for zero and forward speed cases. Vertical force appears about equal at both test depths for a velocity of -0.762 m/sec (-2.5 f.t/sec). As seen in the drag force data, there is an apparent difference between the data results and theoretical results, but the behavior of the trends between cases at different speed are similar. The data trends agree with Cummins' theory in that vertical force increases with increased speed.

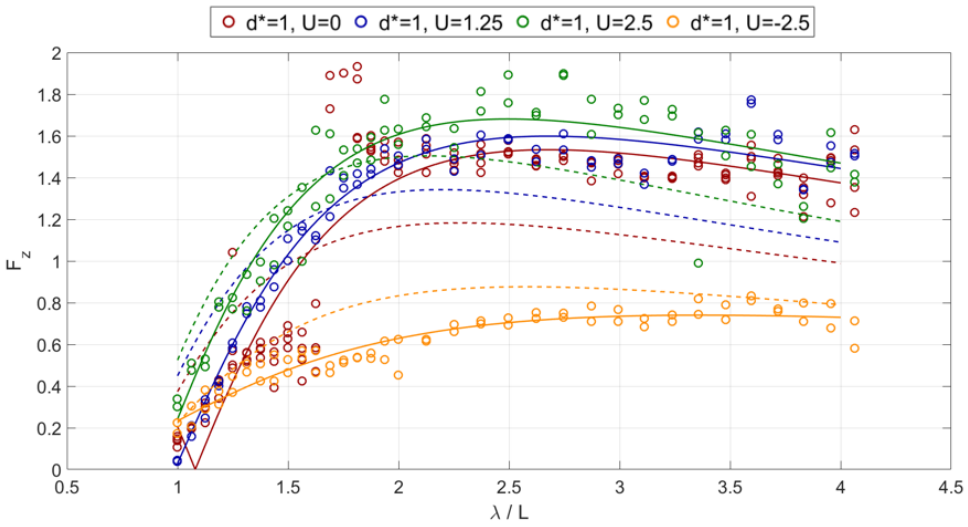

Figure 24. Vertical force results for model with hemispheric end caps at a nondimensional depth of 1.0

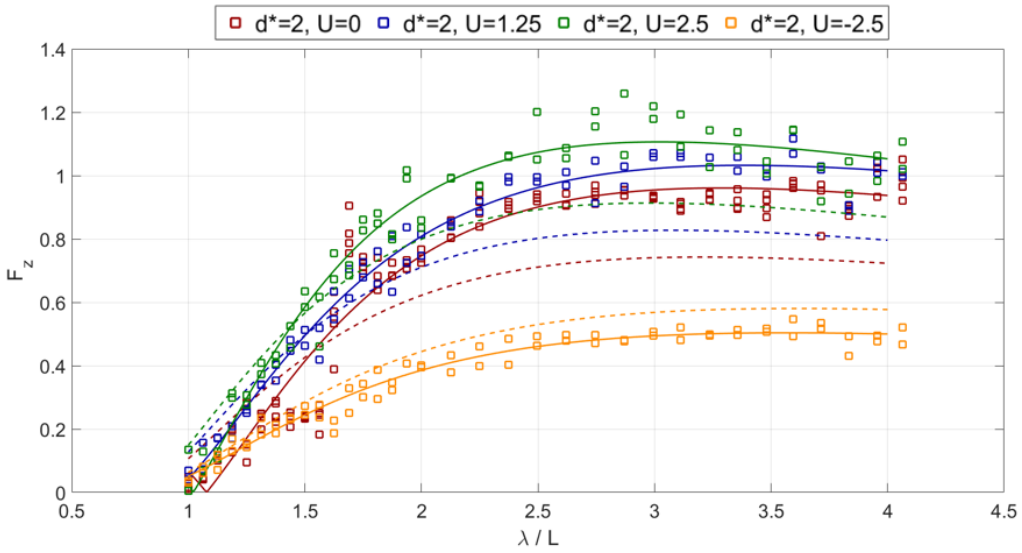

Figure 25. Vertical force results for model with hemispheric end caps at a nondimensional depth of 2.0

The comparison of pitch moments with the model at different speeds is shown in Figure 26 and 27 with the same color formatting as the vertical forces. Again, the data quality decreases with increasing velocity. Between the two depths, the model experiences

more pitch moment at a nondimensional depth of 1.0 with the zero speed and forward speed cases across the tested frequency spectrum. For both depths, there is a clear increase in pitch moment when the model has forward velocity. Due to the scatter, it is not quite obvious whether increasing the velocity from 0.381 to 0.762 m/sec (1.25 ft./sec to 2.5 ft./sec) impacted the pitch moment. A more noticeable increase in pitch moment is expected to be observed given a more dramatic increase in carriage velocity, but higher carriage velocities were unable to be tested due the limited length of the tank.

Theoretical results appear to considerably under predict the pitch moment for forward speed cases. It is possible that the theoretical results for pitch moment are not valid for forward speed cases and that viscous effects cannot be ignored. It is also possible that the experimental setup is inadequate and introduces a lot of inaccuracies in the data collection. This is explained more in Section IV.D., but essentially, the reason for the under prediction in pitch moment is uncertain due to the amount and quality of data.

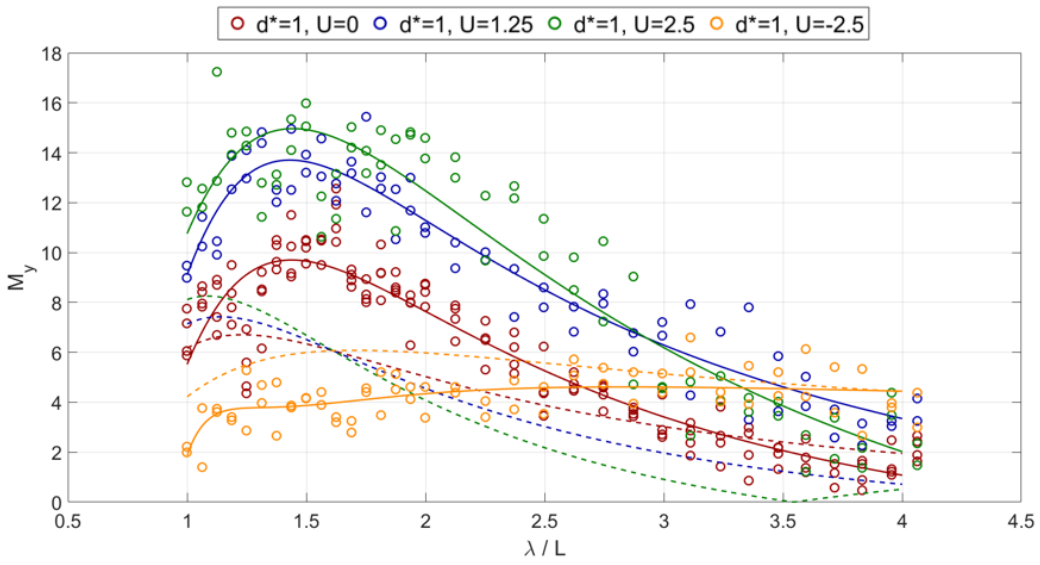

Figure 26. Pitch moment results for model with hemispheric end caps at a nondimensional depth of 1.0

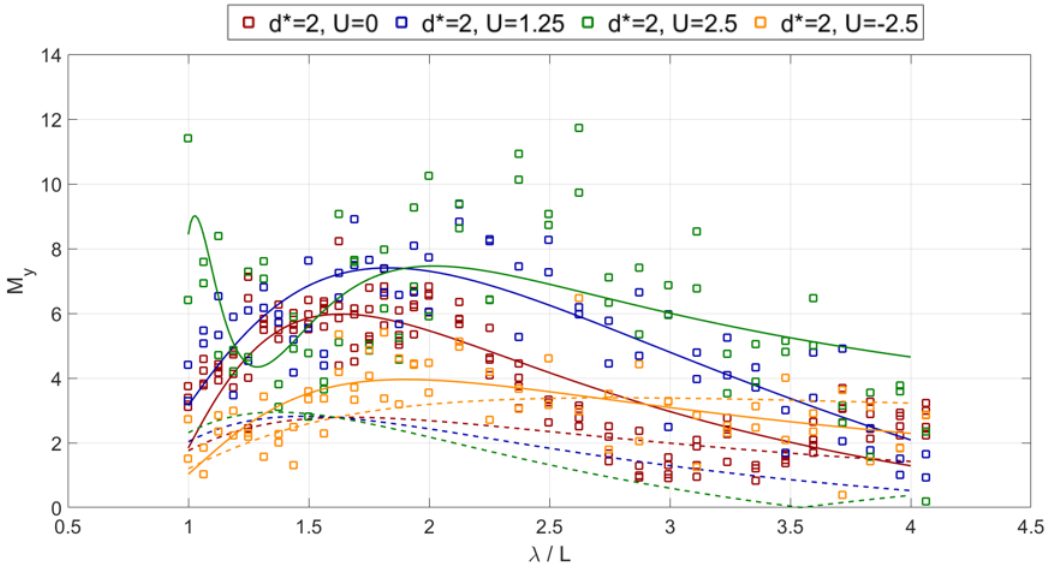

Figure 27. Pitch moment results for model with hemispheric end caps at a nondimensional depth of 2.0

B. FLAT FACED GEOMETRY COMPARISON

1. Comparison of Oscillating Load Amplitudes Due to Speed and Depth

The drag force, vertical force, and pitch moment data for this geometry is shown in the Appendix A and displays very similar results to the hemispherical end cap geometry. It is evident that scatter increases with model velocity, and drag force is overall greater when the model is at a shallower depth. At both depths, the drag force decreases with forward velocity across the tested frequency spectrum. A graphical comparison between the two geometries is shown in Figure 28.

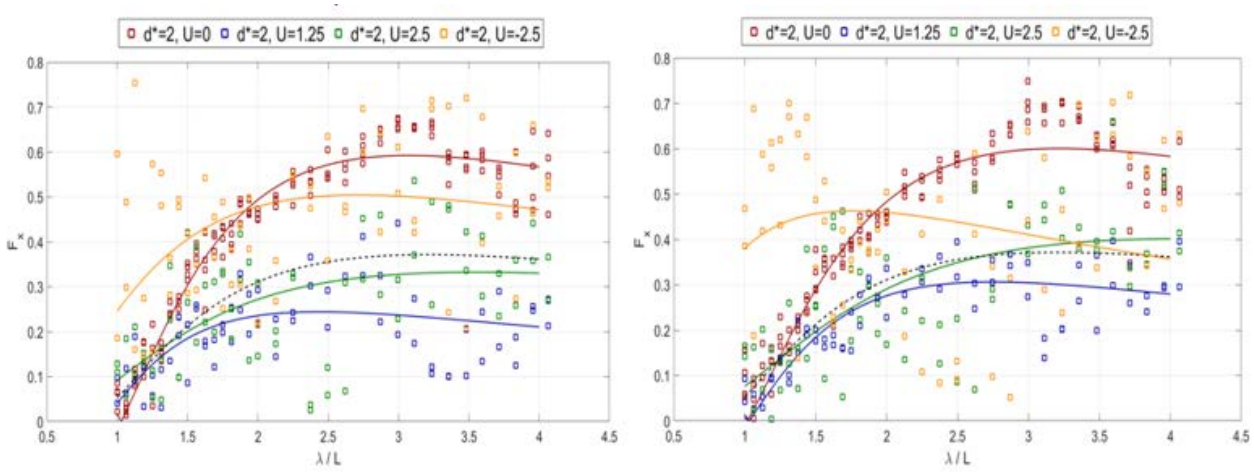

Figure 28. Drag force for hemisphere (left) vs. flat face (right) end cap geometry

For vertical force, the flat faced end cap vertical force data is graphically compared to the hemisphere data in Figure 29. It is possible that the geometry slightly affects the vertical force, but that is not clear from the data due to the scatter.

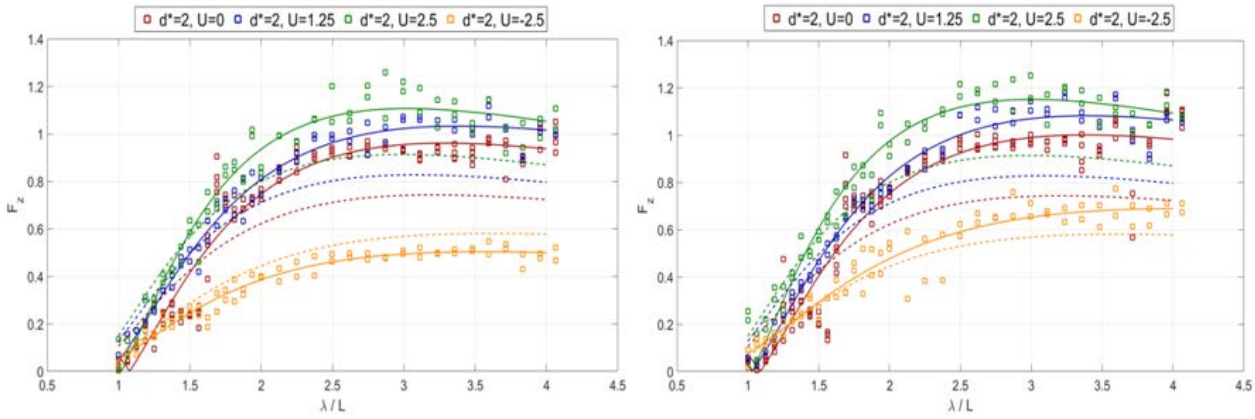

Figure 29. Vertical force for hemisphere (left) vs. flat face (right) end cap geometry

The pitch moment between the two tested depths are shown in Figure 30. For a nondimensional depth of 1.0, there is an obvious shift in the data between the different speeds and that the pitch moment increases with velocity. That is not as clear in the results

for a nondimensional depth of 2.0. At this depth, we note similar pitch moments at zero speed and at velocity of 0.381 m/sec (1.25 ft./sec) at nondimensional wavelengths between 1 and 2. However, there seems to be a more obvious but slight increase in pitch moment for a velocity of 0.762 m/sec (2.5 ft./sec). Unlike what was observed in the drag force and vertical force, difference in end cap geometries appear to have a greater impact on the pitch moment.

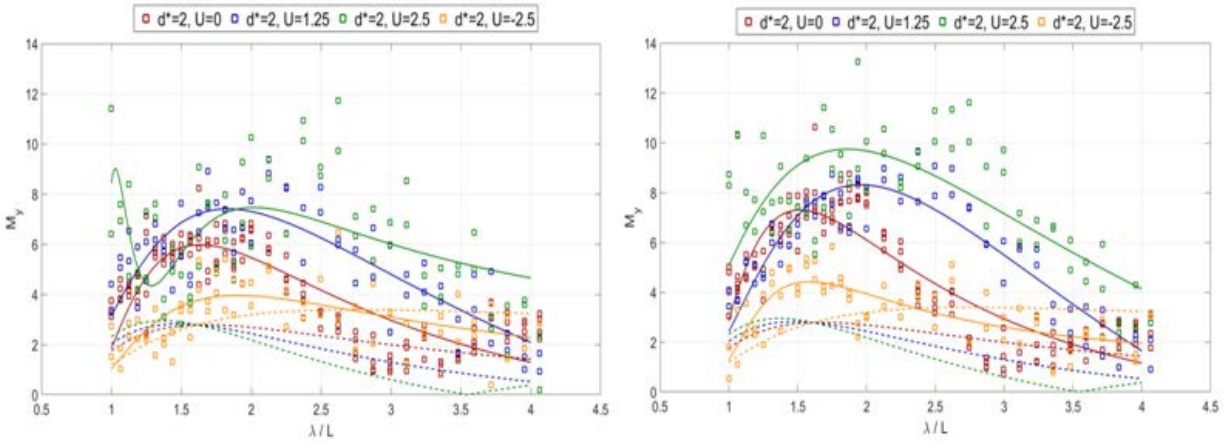

Figure 30. Pitch moments for hemisphere (left) vs. flat face (right) end cap geometry

C. SOURCES OF ERROR

1. Noise in Moving Carriage and Wedge

The plunging wedge structure is directly fixed to the wave tank structure. The carriage motor, platform, and pulley system is also secured to the wave tank structure. All the noise and vibrations associated with all those mechanically moving parts are translated into the moving carriage system. Furthermore, they are measured by sensors that are also impacted by the noise in the system since the load cell sensor and the ultrasonic probes are all coupled to the wave tank structure via different structural members. Although steps have been taken, such as carriage platform strengthening and wedge strengthening that have improved the noise in measurements, it is still not a perfect system. The additional noise introduces imprecisions in the data measurements.

2. Sampling Time

The length of the tow tank provided limitations. The tank length resulted in about 20 ft of usable constant speed run space. This takes into account the space occupied by the wave wedge, carriage fixture, and the inclined perforated sheets at the end. At 2.5 f.t/sec carriage speeds, this resulted in about 8 seconds of run time. However, that run time contained the end portion of the decaying transient caused by starting the carriage. Therefore, the steady-state portion of those runs equated to even less time of useful data. The small frame size at a sampling rate of 50 Hz coupled with the noise associated with the plunging wedge and moving carriage speed introduced inaccuracies in determining signal amplitudes in the data analysis routine.

3. Manual Determination of Steady State

The load-time history of each run had to also be observed in order to determine the true steady-state of the profile run. The carriage at steady-state velocity did not necessarily mean that the drag force and pitch moment were also at steady state. It appeared that the drag force and pitch moment were still in a transient state after the velocity was observed to reach steady-state. The position versus time, drag force versus time, and pitch moment versus time graphs all had to be analyzed in order to determine the point where all measurements reached steady state. Visually determining steady-state velocity was easier and clearer than determining steady-state drag force and pitch moment. For drag force and pitch moment, steady-state was assumed to be when the load versus time graph reached a constant amplitude and frequency. Constant amplitude and frequency was determined by visual inspection. This was not as obvious and possibly introduced inaccuracies in determining drag force and pitch moment in the data analysis.

Figure 29 shows an example of what part of a run data would be assumed to be in steady-state and further used for data reduction and analysis. For runs at 2.5 ft./sec moving through shorter wavelengths, the pitch moment was generally observed to take more time to reach steady-state. In some cases, the pitch moment never reached steady-state, and the carriage had to be stopped due to limited tow tank space. For these cases, the chosen steady-state data had varying amplitudes which is also apparent in Figure 31. Applying the data

reduction process described in Section III.A to this quality of data over a small sample frame size undoubtedly resulted in imprecise pitch moment amplitude data.

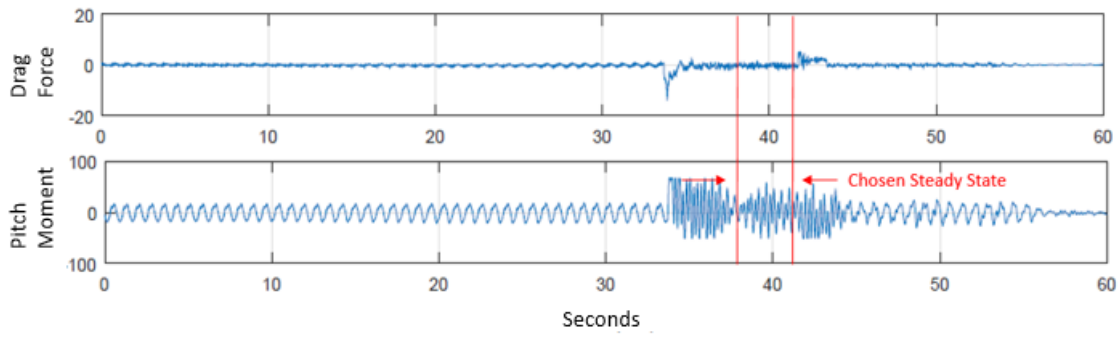

Figure 31. Chosen steady-state used for data analysis from load-time history plot

4. Velocity Accuracy

To measure distance using the position probe, a Plexiglas plate was vertically secured to the top of the carriage to give the probe a good flat-faced target to acquire. The position probe uses ultrasonic sound waves that have a 12-degree conical angle [12]. The ultrasonic wave at the end of the tank covers more than the Plexiglas and reflects off all the flat faces protruding from the carriage and model fixtures. The result is set of returns that can have inaccurate range readings. As the carriage closes in on the sensor during a run, the pulse radius of the ultrasonic waves decrease and ultimately reflects off the Plexiglas surface. When the carriage is in motion, the position is measured and plotted against the elapsed time. Figure 32 shows a plot of carriage position of a desired run versus a run when the ultrasound from the position probe is reflected off of the wrong target surface.

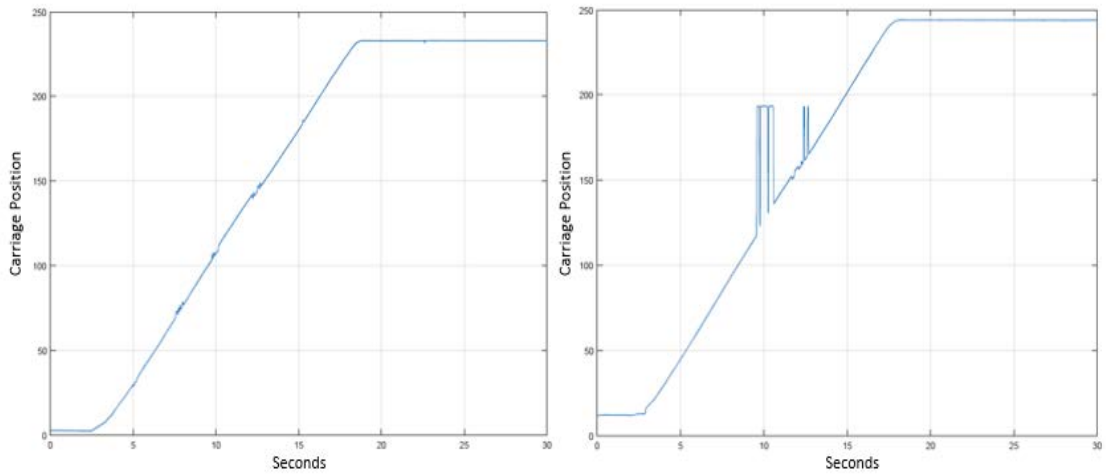

Figure 32. Comparison of carriage position plots resulting from different ultrasonic target acquisition

To calculate velocity, the beginning and end of steady-state speed was visually determined from the position versus time graph in the data cleaning process. The steady-state velocity was assumed to be when the position versus time line looked the most linear between the acceleration and deceleration. The different surfaces that the probe could possibly reflect off of resulted in an imperfectly linear plot with occasionally spikes in the assumed steady-state portion of the graph. A linear curve fit was applied to the assumed steady-state portion in order to calculate the steady state velocity. Figure 33 shows the potential error in determining carriage velocity.

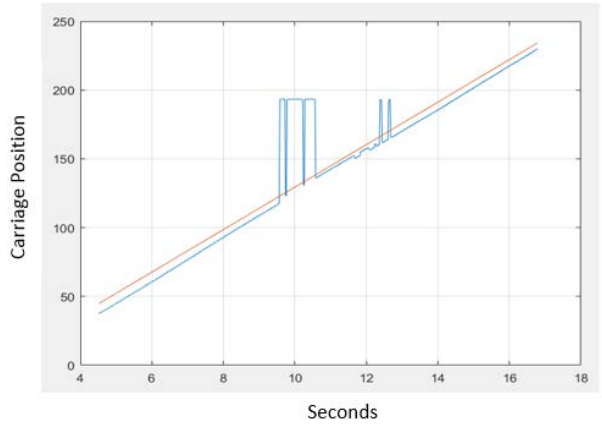

Figure 33. Linear curve fit of carriage velocity

5. Wave Height When Moving

The experimental setup had a total of three ultrasonic probes to measure wave height. Two of those probes were located 0.508 m (20 in.) ahead of the model to measure incoming the wave height and encounter frequency. Due to the limited availability of space on the carriage, the probes were offset from the center shown in Figure 14. The last probe was positioned above the model to measure the wave height as it passed over the model. The desired wave height was 1 inch, but the measured wave heights from the probes were scattered. For the two probes located ahead of the model, the measured wave heights is hypothesized to be the result of interference with energy from the wave reflected from the side of the tank as it propagates. Ideally, these sensors would be positioned in the center of the tank to avoid as much wave interference as possible. For shorter wavelengths, the waves tended to break over the model, and this is likely the reason why the measurement from the probe located above the model was not 5.54 cm (1 in.). Figure 34 shows a wave breaking over the model which could have possible lead to inaccuracies in measuring wave height.

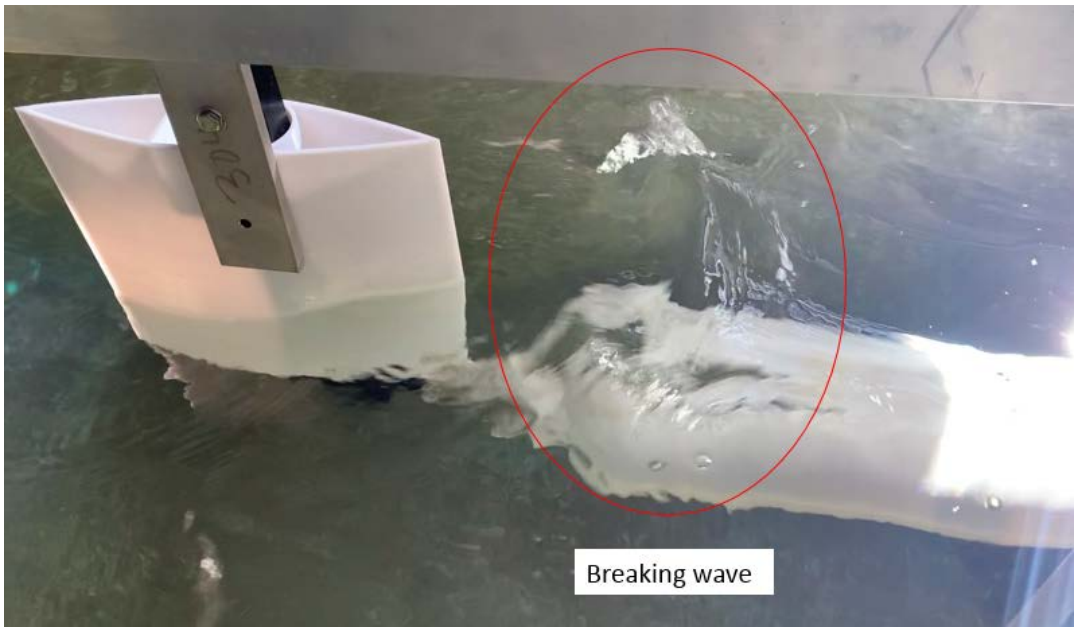

Figure 34. Wave breaking over the model

V. CONCLUSION AND FUTURE WORK

A. CONCLUSION

Forward speed makes the theoretical predictions of oscillatory drag force less accurate. The inviscid potential fluid solution shows that drag force is not dependent on model speed, however, it is apparent from the experimental results that forward speed has an effect on drag force. Therefore, results suggest that viscous effects due to speed are able to alter the wave induced drag forces. The flat faced geometry shows roughly the same oscillatory drag as the hemisphere which indicates that for a given forward speed, oscillatory drag force is not sensitive to the changes in the size and location of the separation region around the model due to end cap geometry.

For vertical force, theoretical predictions do well in predicting the behavioral trends with respect to depth, speed, and wavelength. For zero and forward speed cases, it under predicts the vertical force. For negative speed cases, the theory slightly over predicts the vertical force. Flat face geometry shows similar results to the hemisphere geometry. The presence of a separation region due to forward speed impacts the vertical force but changes to the location and size of the separation region, for a given speed, do not appear to have an impact.

Theory under predicts pitch moment for zero and forward speed cases. Unlike drag and vertical force, changing front face geometry had the most impact on pitch moment. Therefore, the pitching moment was more sensitive to changes to the size and location of the separation region around the model.

B. FUTURE WORK

1. Explore Forward Speed with Varying Pitch Angle

The purpose of this specific study was to explore the effects of forward speed at a pitch of zero. Cummin's theory does not allow for a pitch angle on the body when predicting first-order hydrodynamic loads. Rarely do maritime vessels, including UUVs,

operate with a wave approach angle of zero. Thus, it is very important to understand the effects of varying vessel orientation to the wave for effective real world operations.

2. Explore Forward Speed in Complex Seaways

Whitmer [10] explored the effect of complex seaways, varying wave profiles, in a similar experimental setup at NPS but only for a model at zero speed. Now that NPS has the capability to couple both forward speed and varying wave generation, this would be an important aspect of the complex UUV problem to explore as real world environment guarantees a complex seaway for UUVs on mission.

APPENDIX A. DRAG FORCE, VERTICAL FORCE, AND PITCH MOMENT DATA

The red data is for zero velocity runs, the blue data is for a velocity of 0.381 m/sec (1.25 ft./sec), the green data is for velocity of 0.762 m/sec (2.5 ft./sec), and the yellow data is for a velocity of -0.762 m/sec (-2.5 ft./sec). The solid lines are the curve fits for their respective colors. Positive velocities correspond to head seas and negative velocities correspond to following seas. The dashed lines are the theoretical predictions.

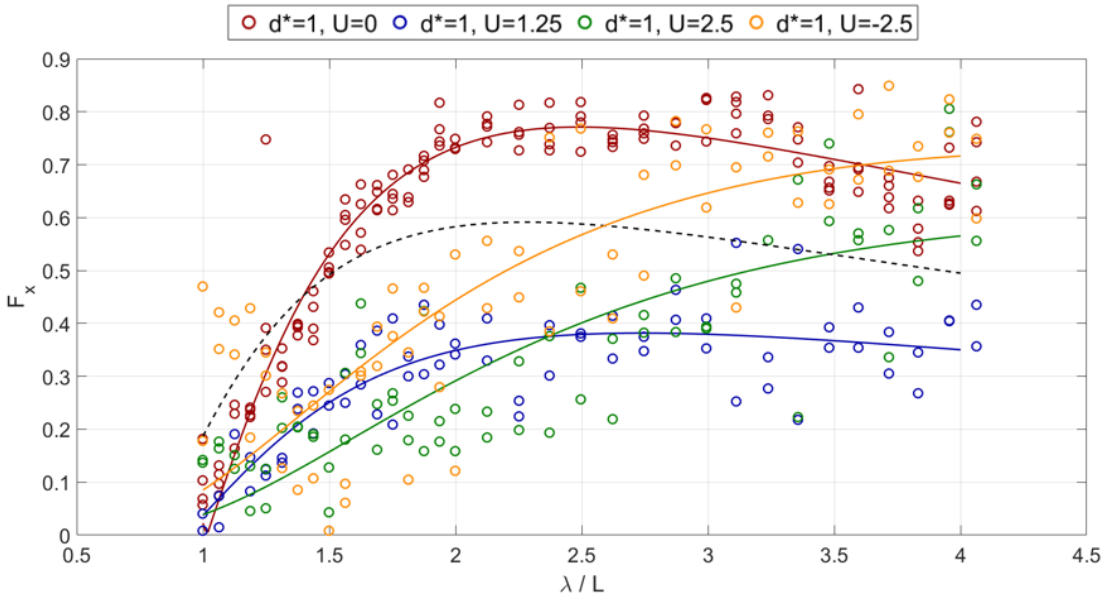

Figure 35. Drag force results for model with hemispheric end caps at a nondimensional depth of 1.0

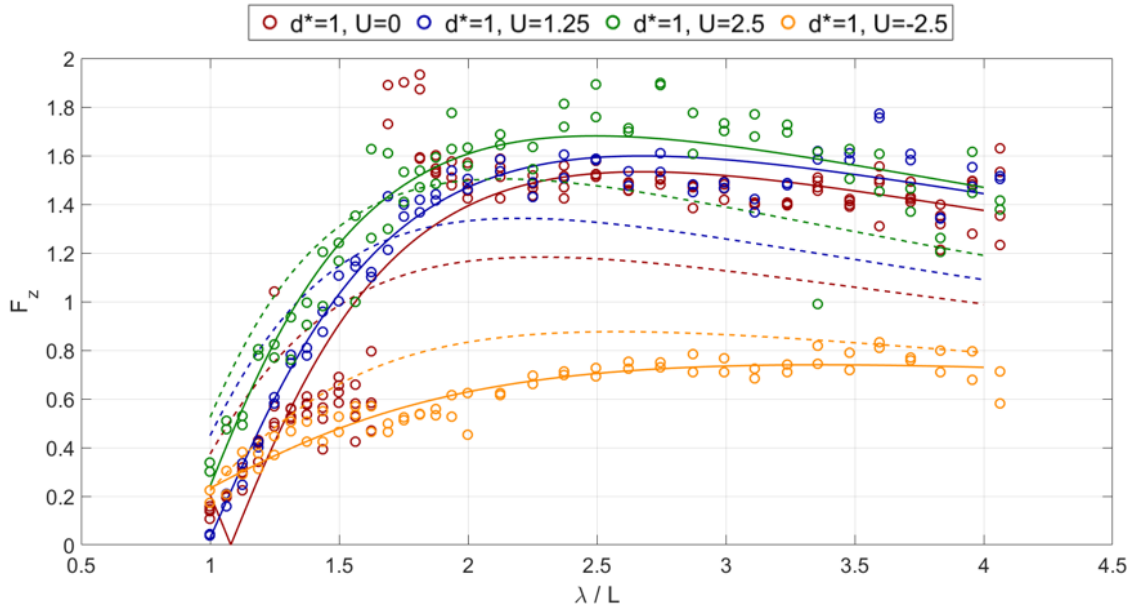

Figure 36. Vertical force results for model with hemispheric end caps at a nondimensional depth of 1.0

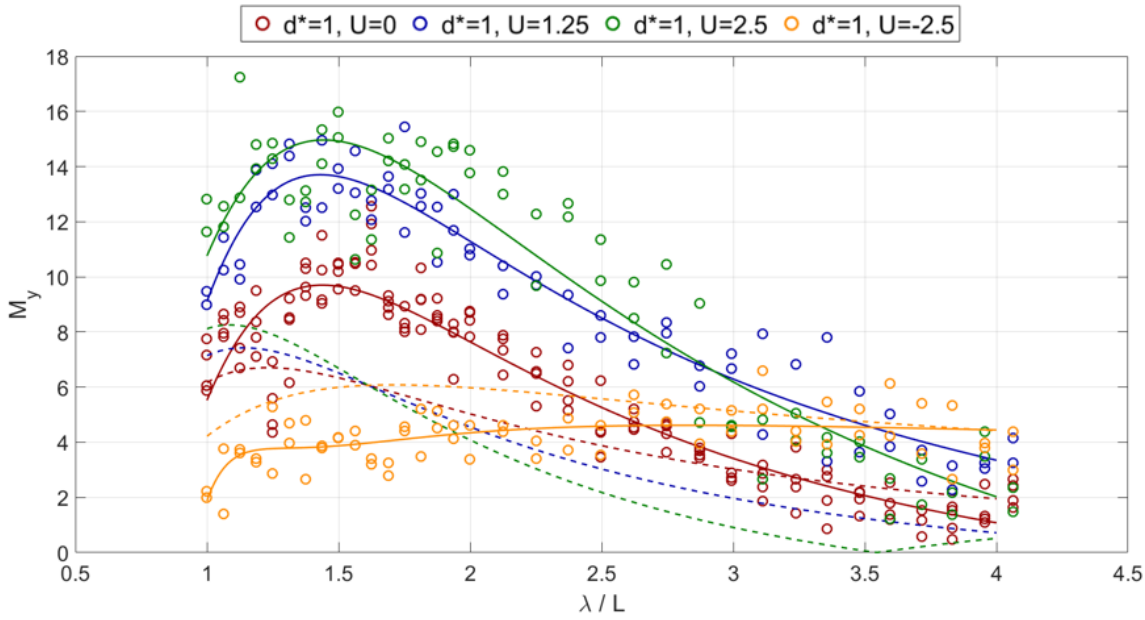

Figure 37. Pitch moment results for model with hemispheric end caps at a nondimensional depth of 1.0

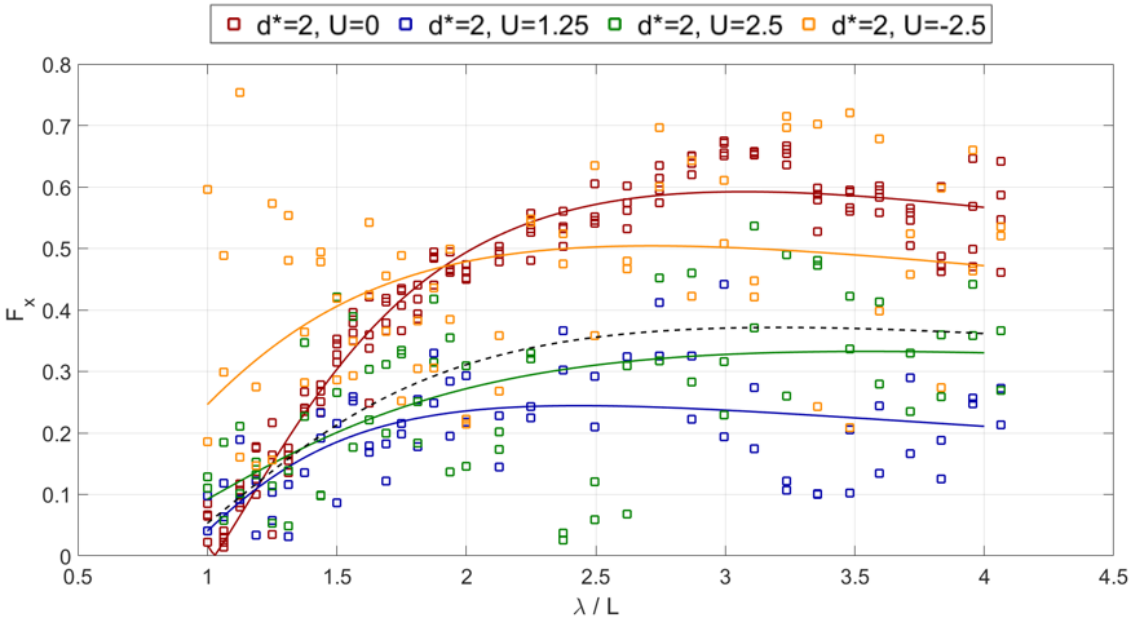

Figure 38. Drag force results for model with hemispheric end caps at a nondimensional depth of 2.0

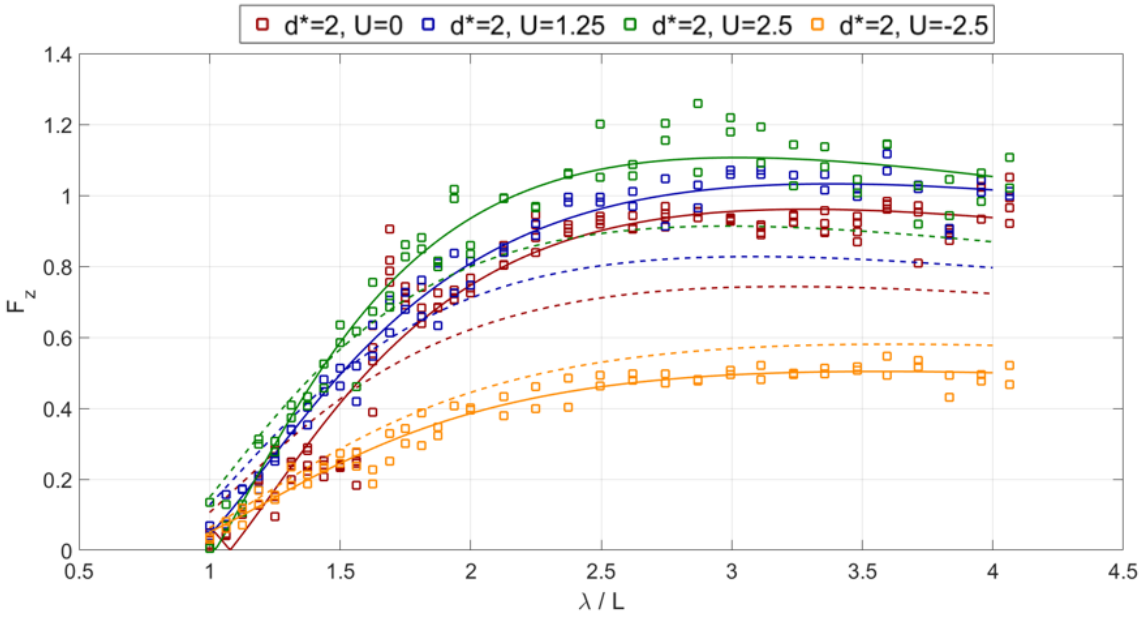

Figure 39. Vertical force results for model with hemispheric end caps at a nondimensional depth of 2.0

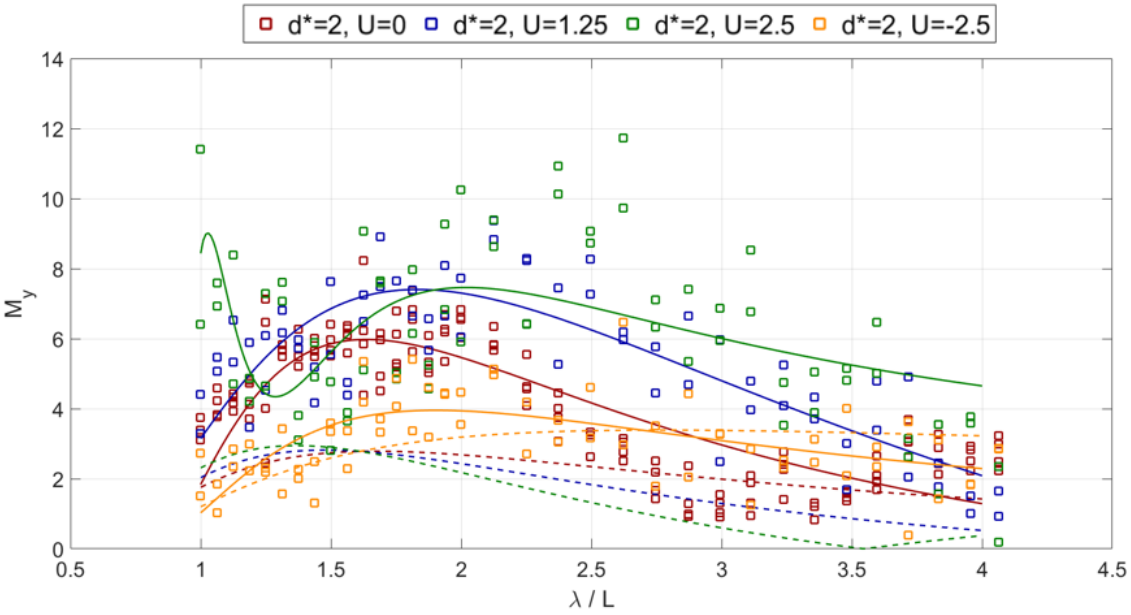

Figure 40. Pitch moment results for model with hemispheric end caps at nondimensional depth of 2.0

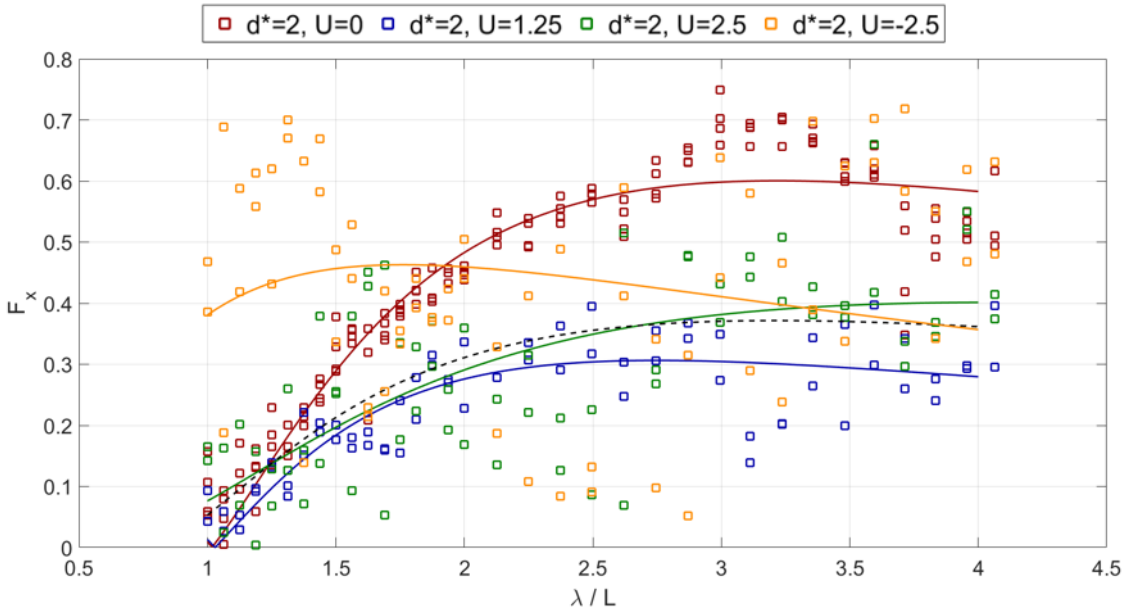

Figure 41. Drag force results for model with flat face end caps at a nondimensional depth of 1.0

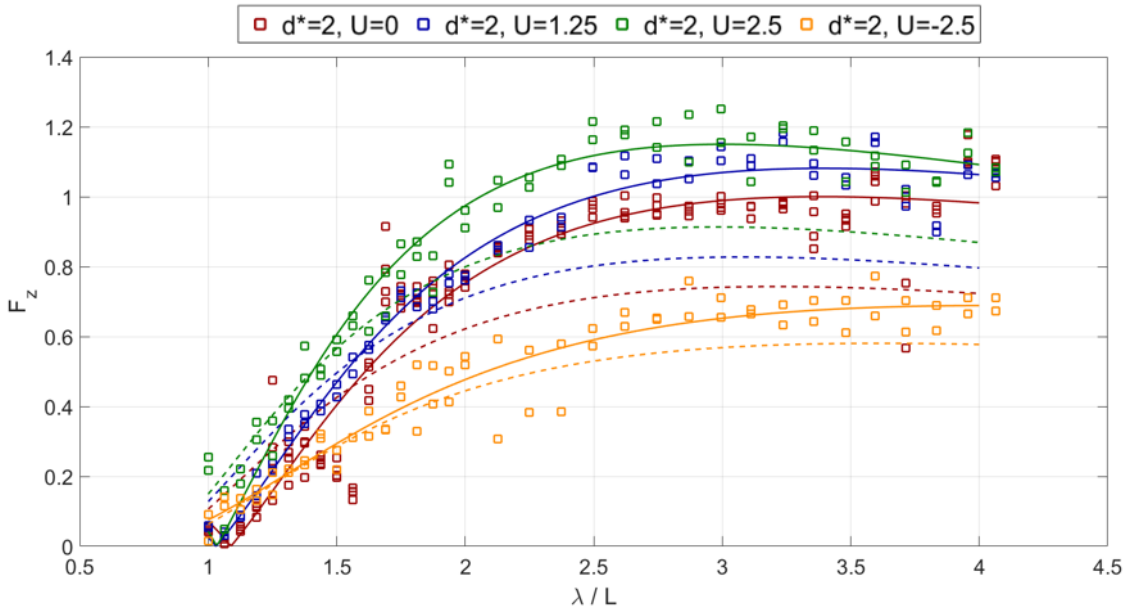

Figure 42. Vertical force results for model with flat face end caps at a nondimensional depth of 1.0

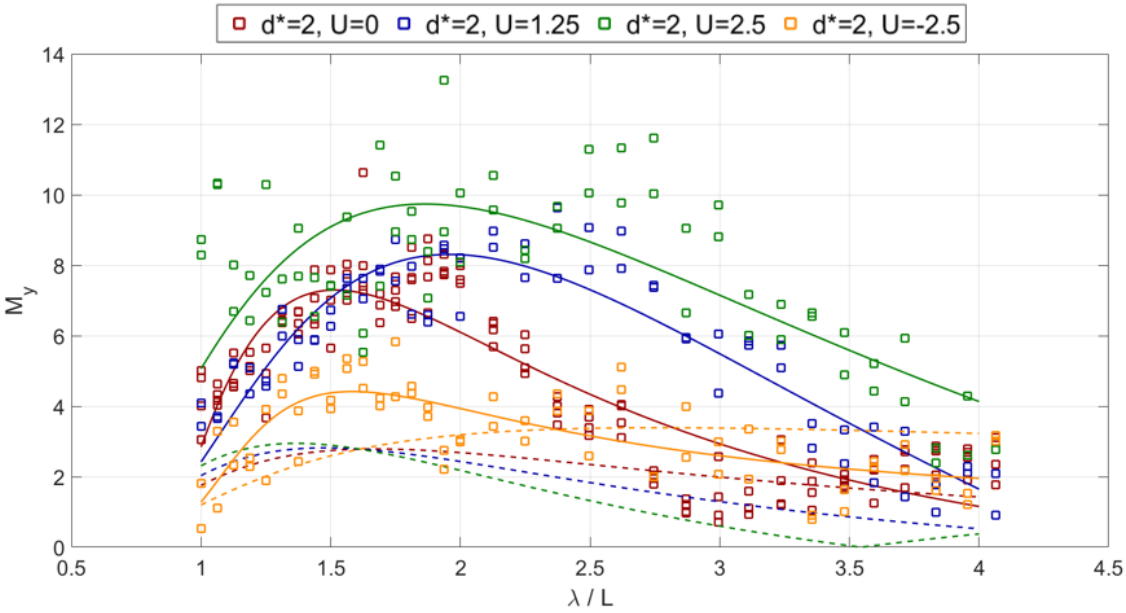

Figure 43. Pitch moment results for model with flat face end caps at a nondimensional depth of 1.0

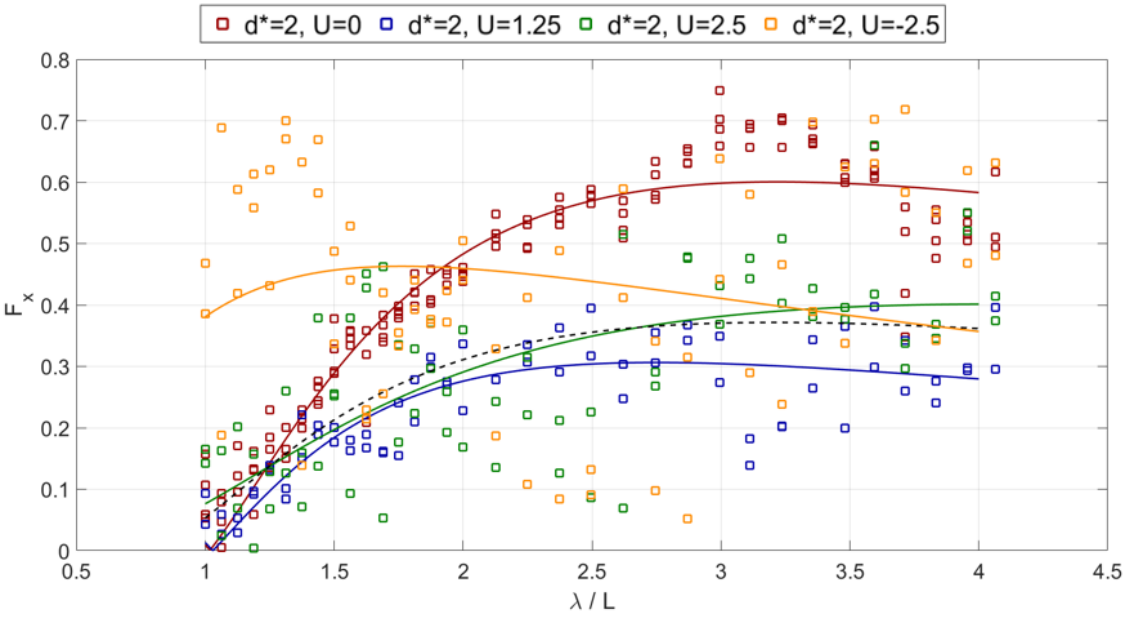

Figure 44. Drag force results for model with flat face end caps at a nondimensional depth of 2.

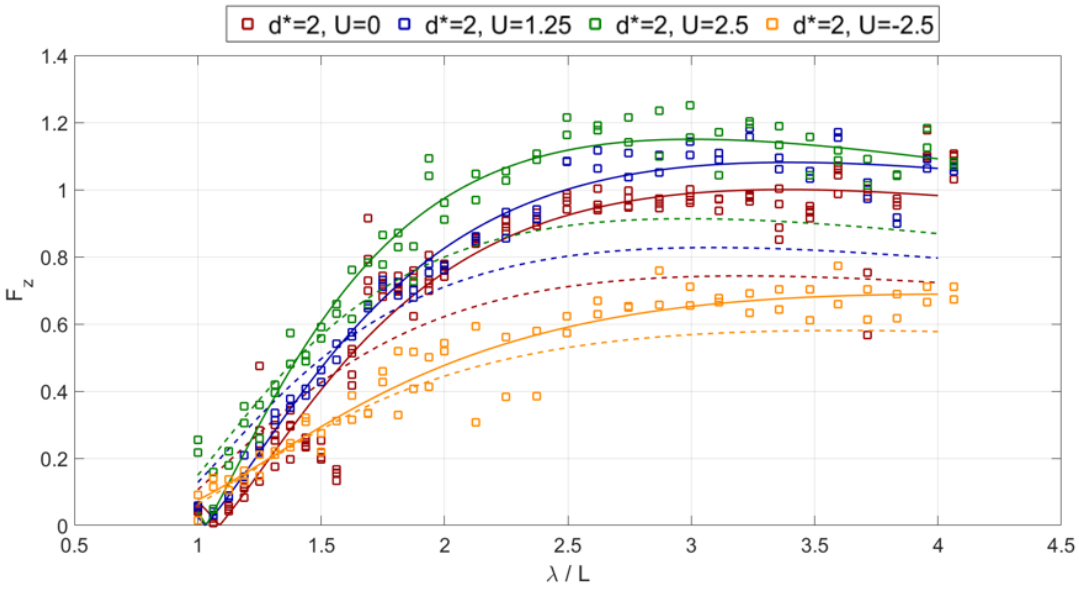

Figure 45. Vertical force results for model with flat face end caps at a nondimensional depth of 2.0

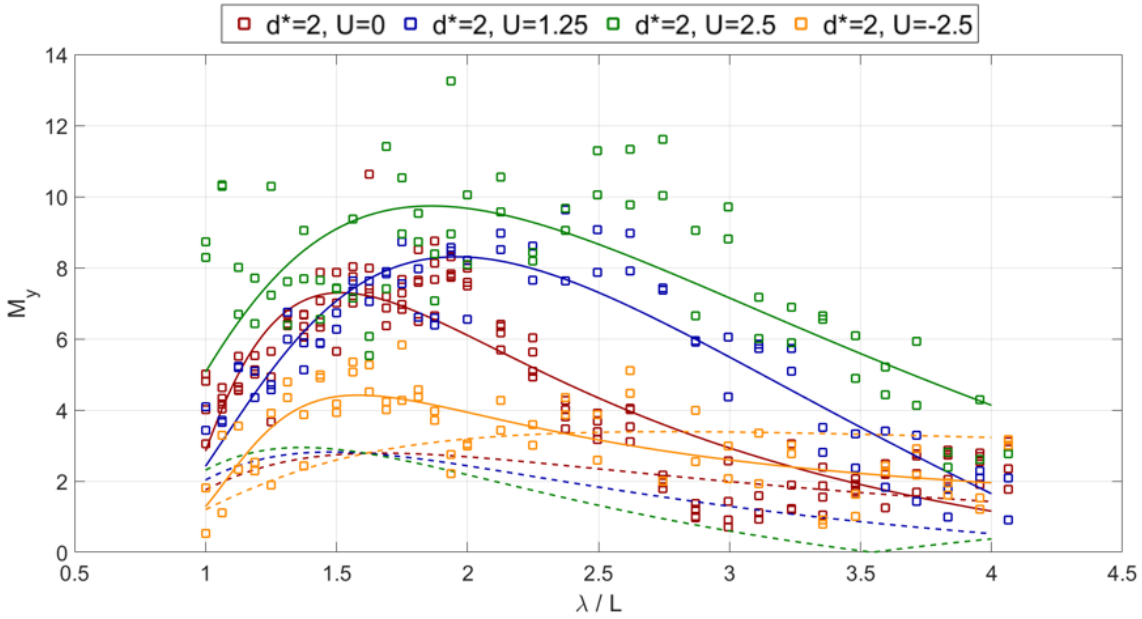

Figure 46. Pitch moment results for model with flat face end caps at a nondimensional depth of 2.0

THIS PAGE INTENTIONALLY LEFT BLANK

APPENDIX B. CONFIDENCE LEVELS WITH DATA

The drag force and vertical force data with confidence levels are plotted here. The solid line is the curve fit, the darker dashed lines show the 95% confidence interval bound of the curve-fit, and the lighter dashed lines show the prediction interval on the curve fit. The confidence interval bound is the confidence on the location of the curve-fit, and the prediction interval fit is the confidence on where the data points will fall relative to the curve fit.

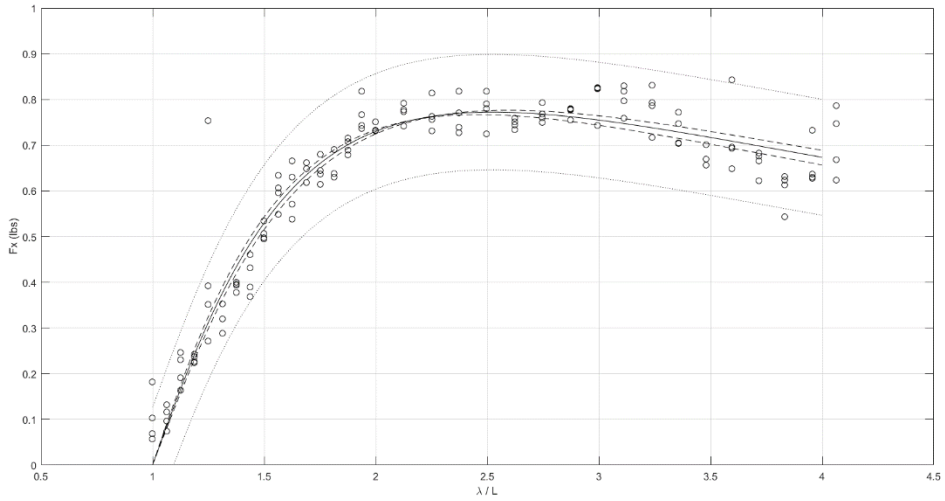

Figure 47. Drag force results for model with hemisphere end caps at a nondimensional depth of 1.0 at zero speed

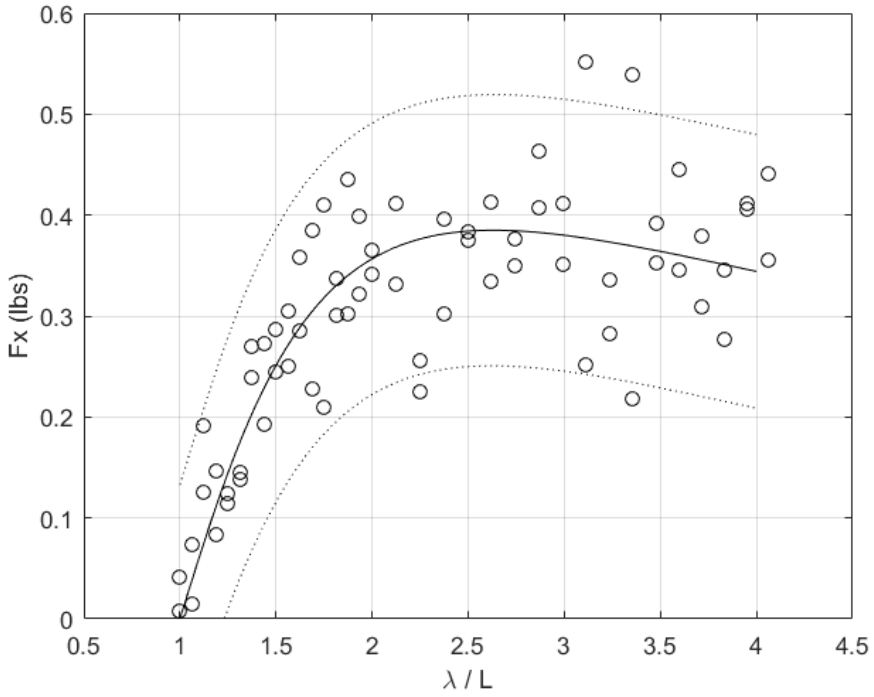

Figure 48. Drag force results for model with hemisphere end caps at a nondimensional depth of 1.0 at 0.381 m/sec (1.25 ft./sec)

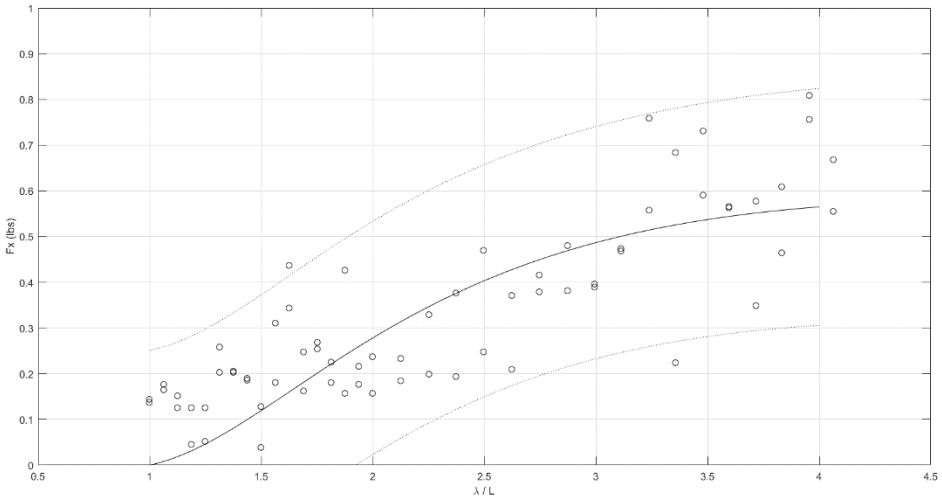

Figure 49. Drag force results for model with hemisphere end caps at a nondimensional depth of 1.0 at 0.762 m/sec (2.5ft.sec)

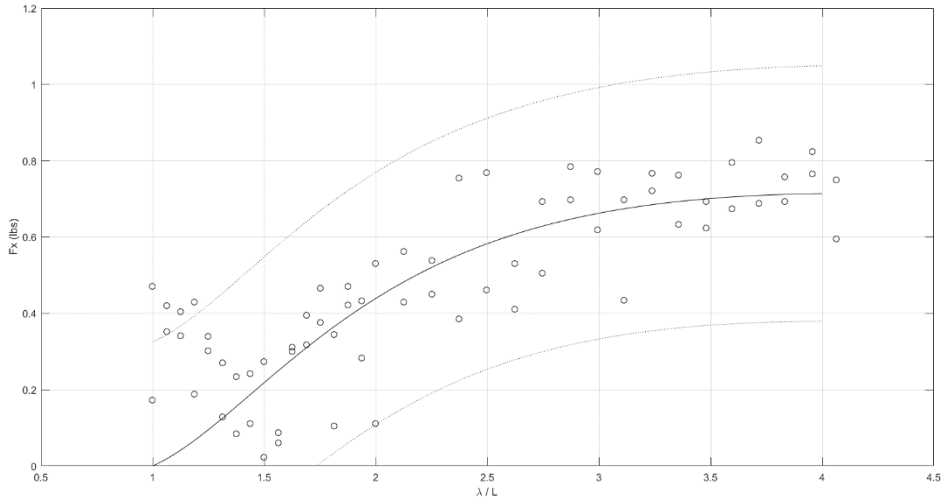

Figure 50. Drag force results for model with hemisphere end caps at a nondimensional depth of 1.0 at -0.762 m/sec (-2.5 ft./sec)

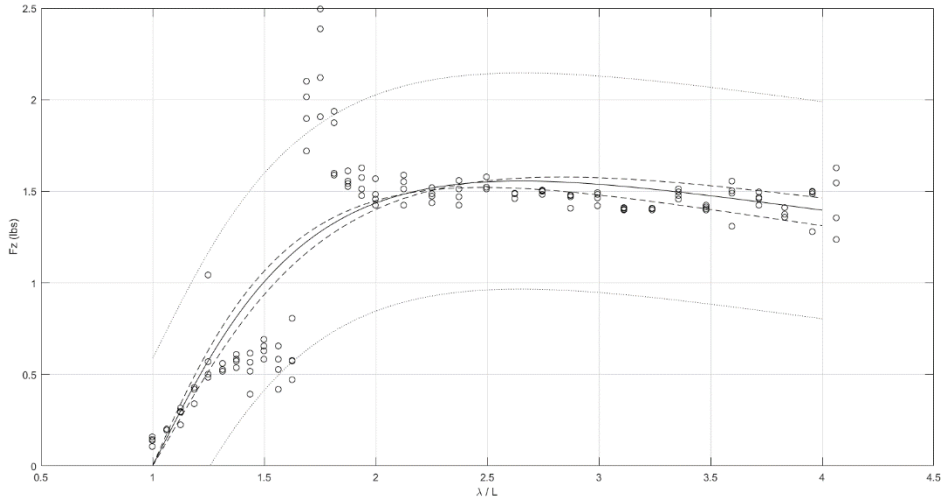

Figure 51. Vertical force results for model with hemisphere end caps at a nondimensional depth of 1.0 at zero speed

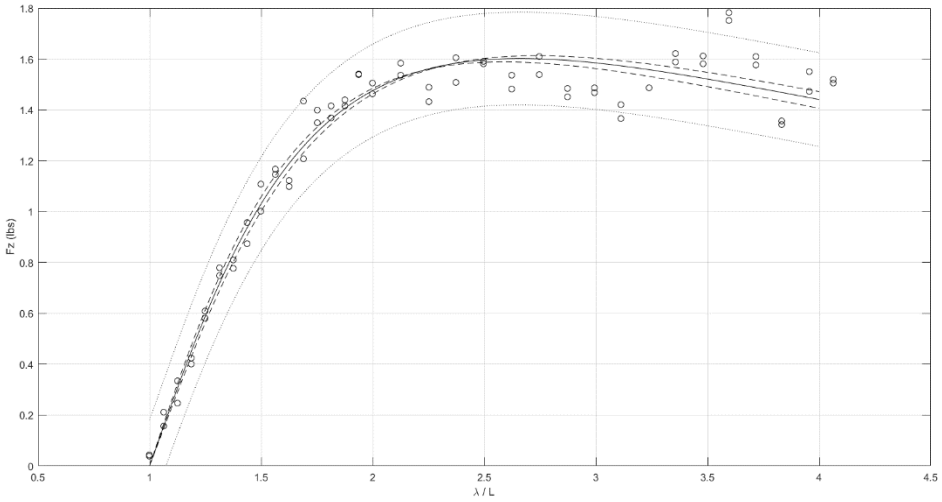

Figure 52. Vertical force results for model with hemisphere end caps at a nondimensional depth of 1.0 at 0.381 m/sec (1.25 ft./sec)

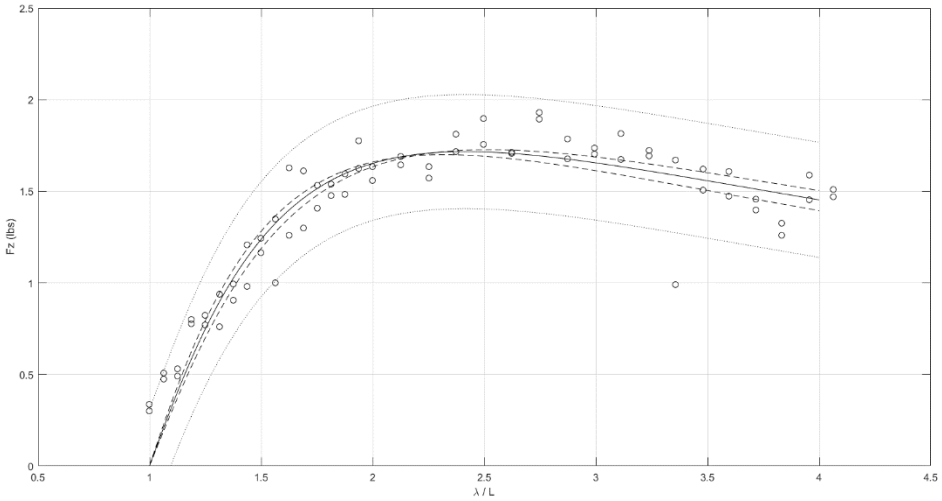

Figure 53. Vertical force results for model with hemisphere end caps at a nondimensional depth of 1.0 at 0.762 m/sec (2.5 ft./sec)

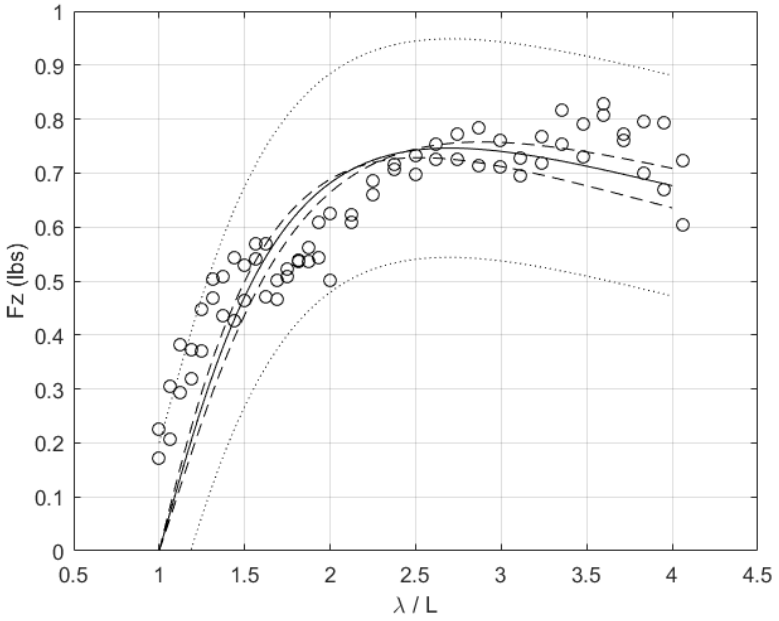

Figure 54. Vertical force results for model with hemisphere end caps at a nondimensional depth of 1.0 at -0.762 m/sec (-2.5 ft./sec)

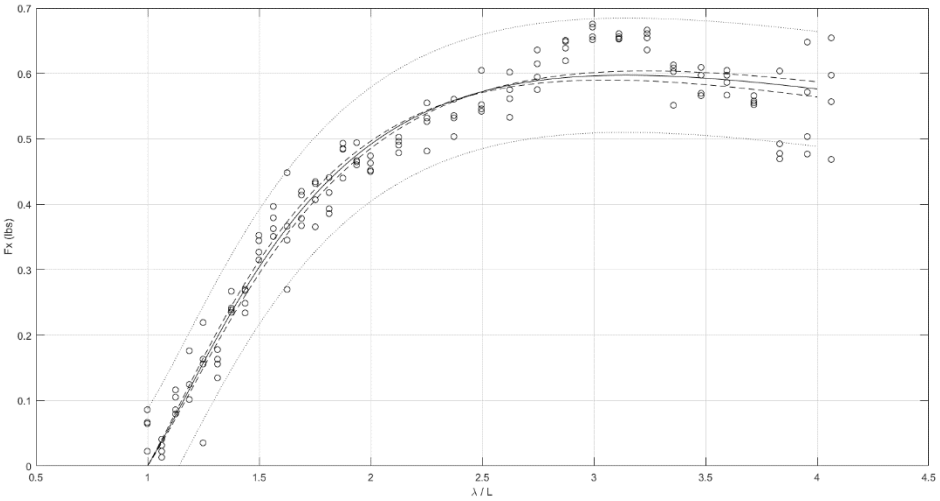

Figure 55. Drag force results for model with hemisphere end caps at a nondimensional depth of 2.0 at zero speed

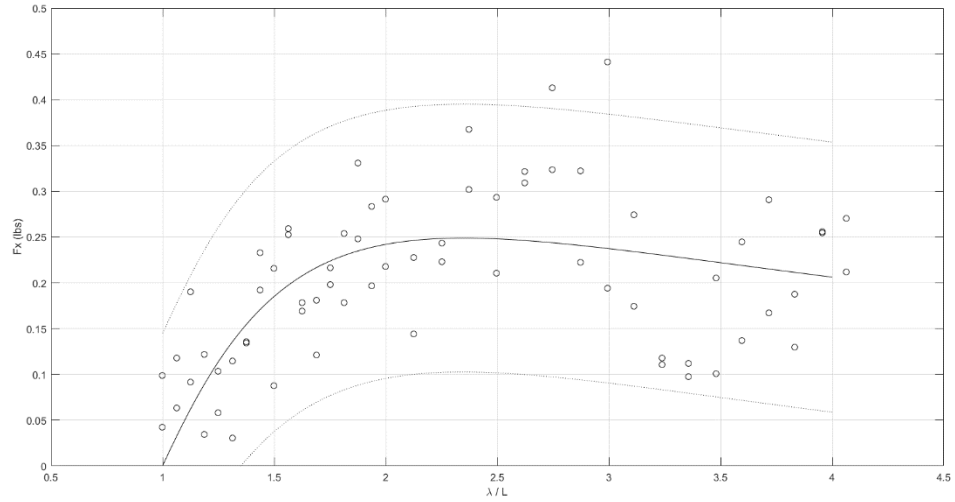

Figure 56. Drag force results for model with hemisphere end caps at a nondimensional depth of 2.0 at 0.381 m/s (1.25 ft./sec)

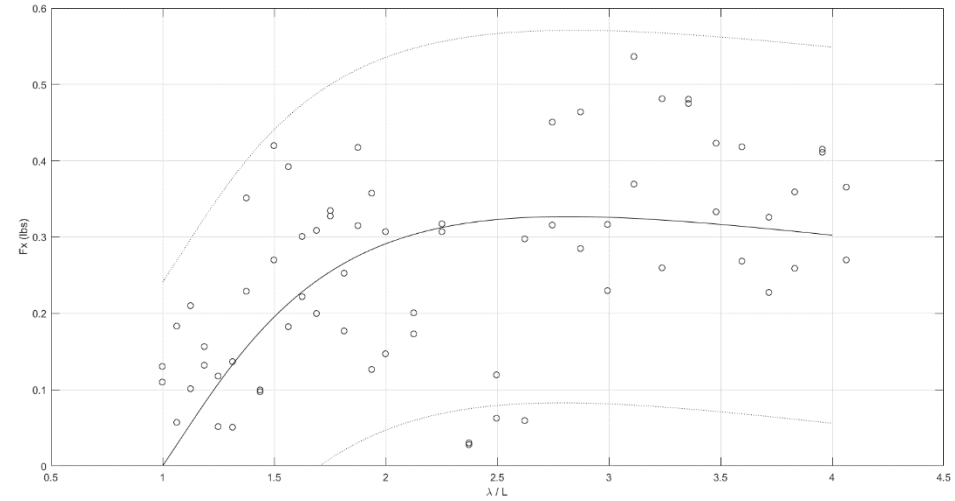

Figure 57. Drag force results for model with hemisphere end caps at a nondimensional depth of 2.0 at 0.762 m/sec (2.5 ft./sec)

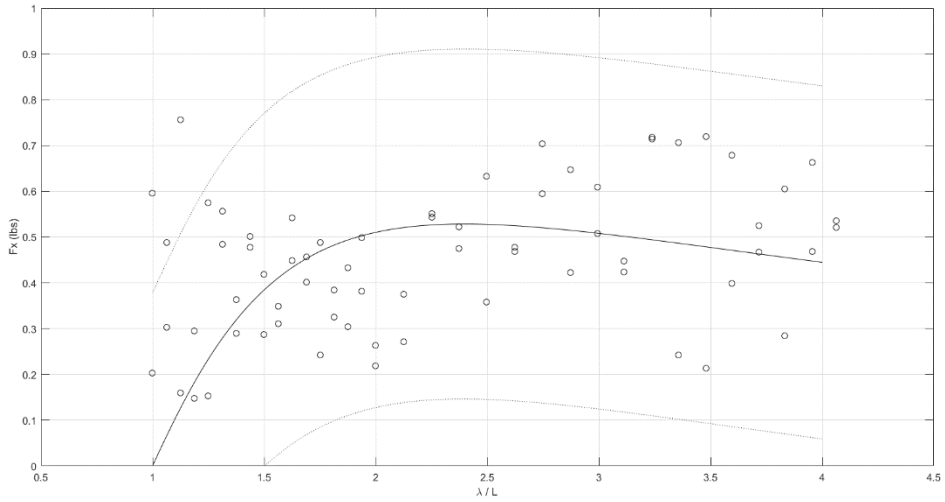

Figure 58. Drag force results for model with hemisphere end caps at a nondimensional depth of 2.0 at -0.762 m/sec (-2.5 ft./sec)

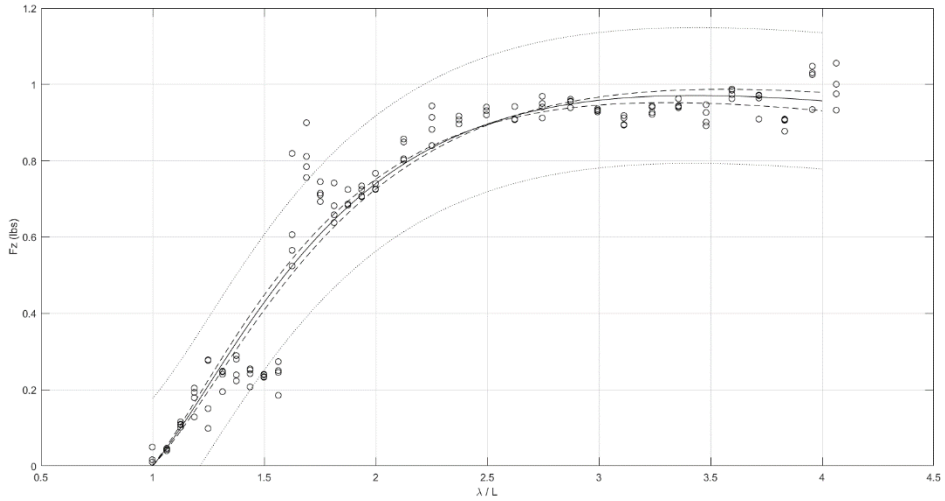

Figure 59. Vertical force results for model with hemisphere end caps at a nondimensional depth of 2.0 at zero speed

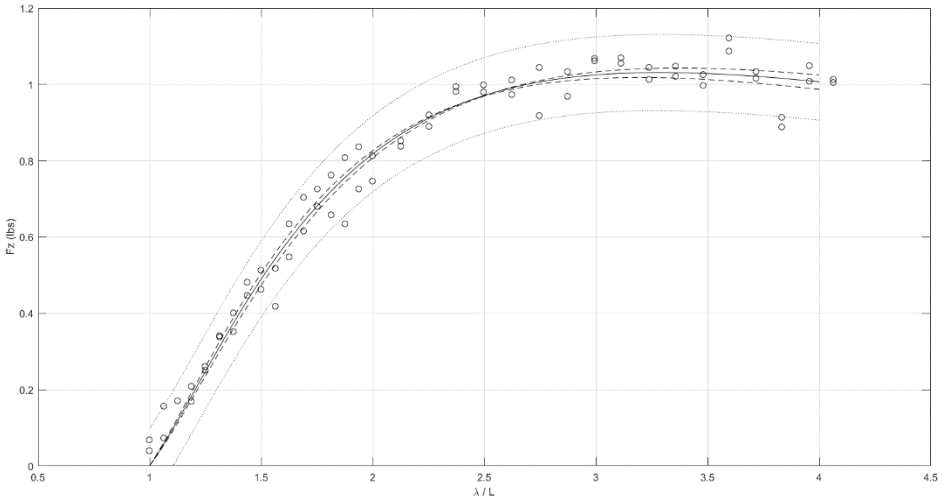

Figure 60. Vertical force results for model with hemisphere end caps at a nondimensional depth of 2.0 at 0.381 m/sec (1.25 ft./sec)

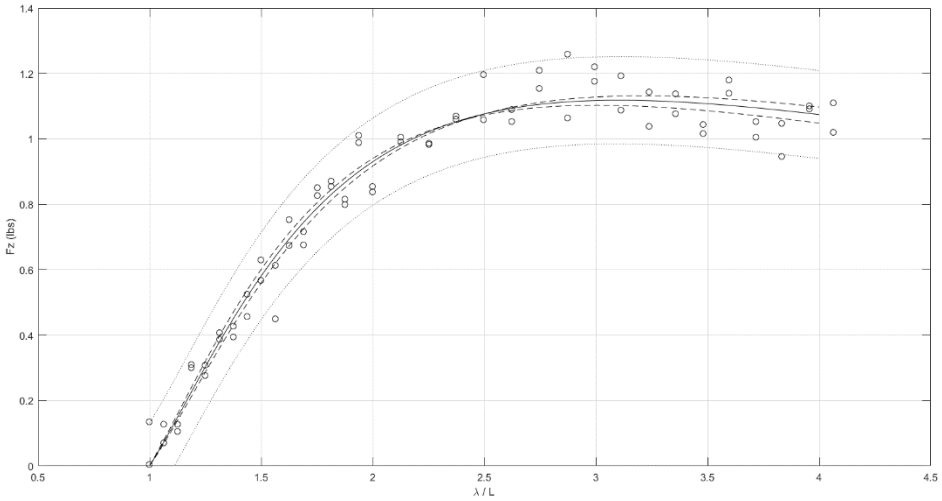

Figure 61. Vertical force results for model with hemisphere end caps at a nondimensional depth of 2.0 at 0.762 m/sec (2.5 ft./sec)

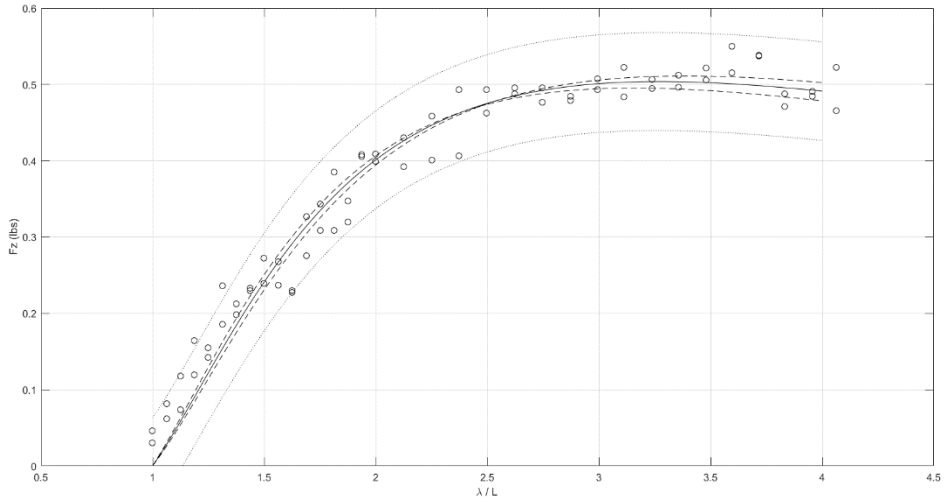

Figure 62. Vertical force results for model with hemisphere end caps at a nondimensional depth of 2.0 at -0.762 m/sec (-2.5 ft./sec)

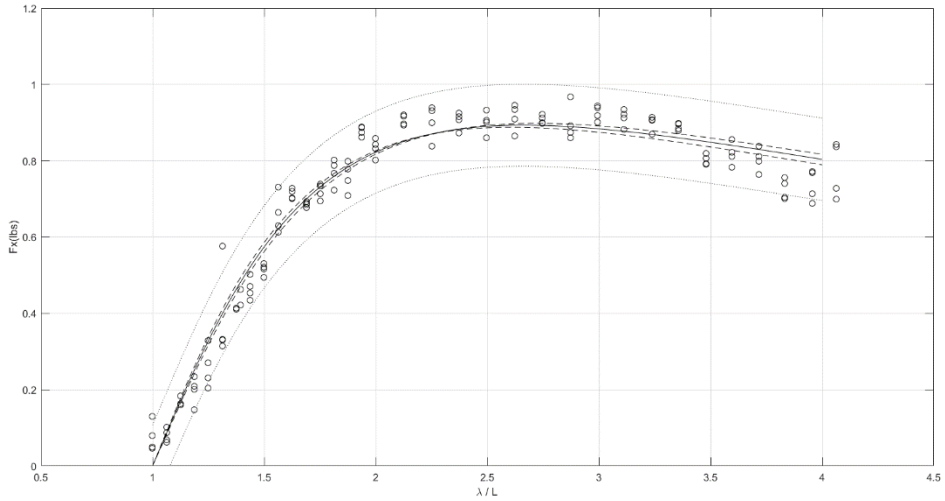

Figure 63. Drag force results for model with flat face end caps at a nondimensional depth of 1.0 at zero speed.

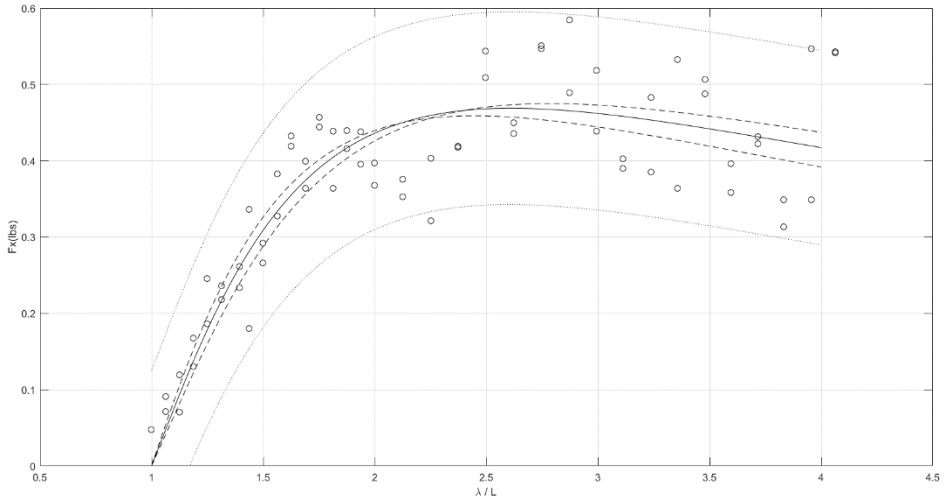

Figure 64. Drag force results for model with flat face end caps at a nondimensional depth of 1.0 at 0.381 m/sec (1.25 ft./sec)

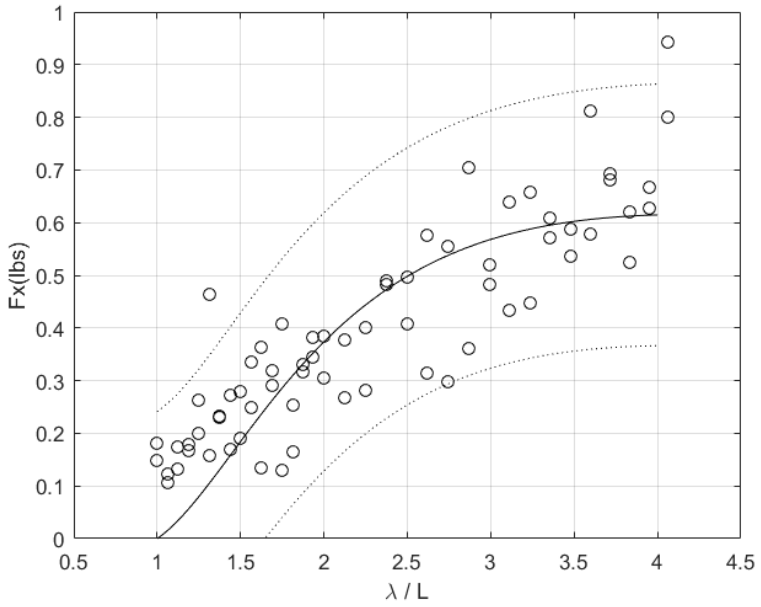

Figure 65. Drag force results for model with hemispheric end caps at a nondimensional depth of 1.0 at 0.762 m/sec (2.5 ft./sec)

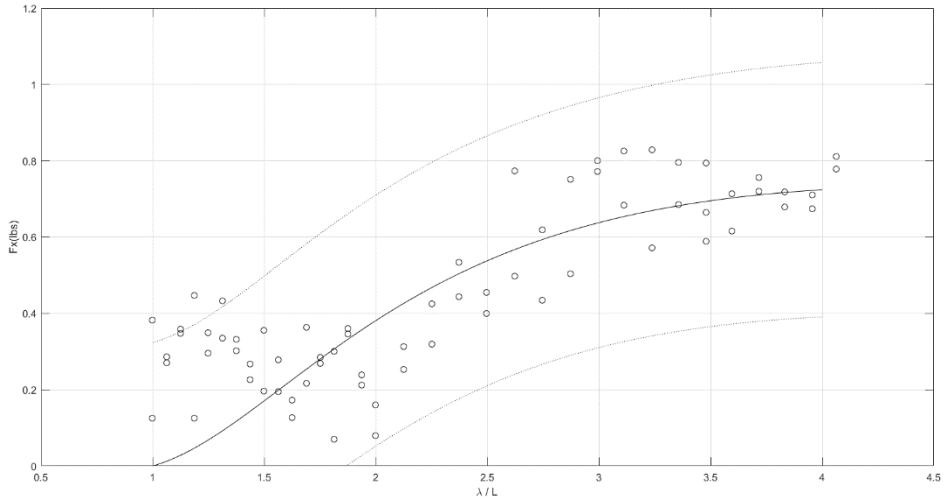

Figure 66. Drag force results for model with flat face end caps at a nondimensional depth of 1.0 at -0.762 m/sec (-2.5 ft./sec)

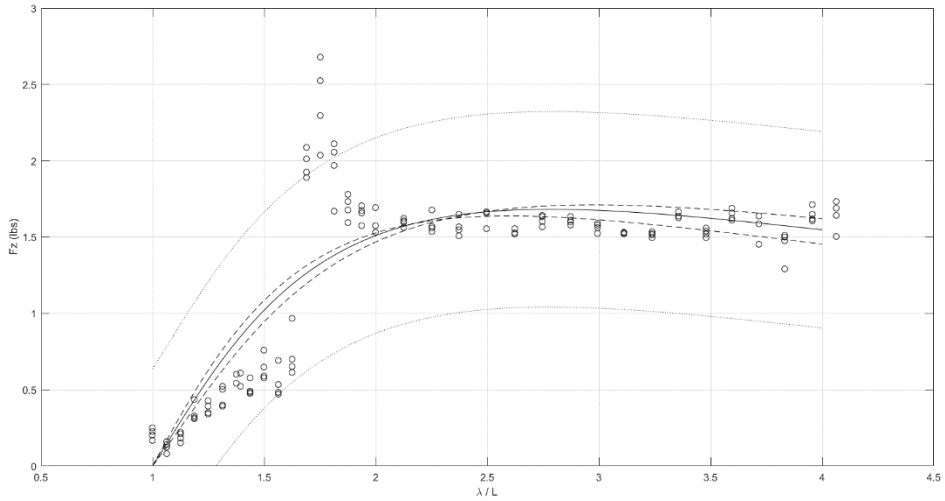

Figure 67. Vertical force results for model with flat face end caps at a nondimensional depth of 1.0 at zero speed

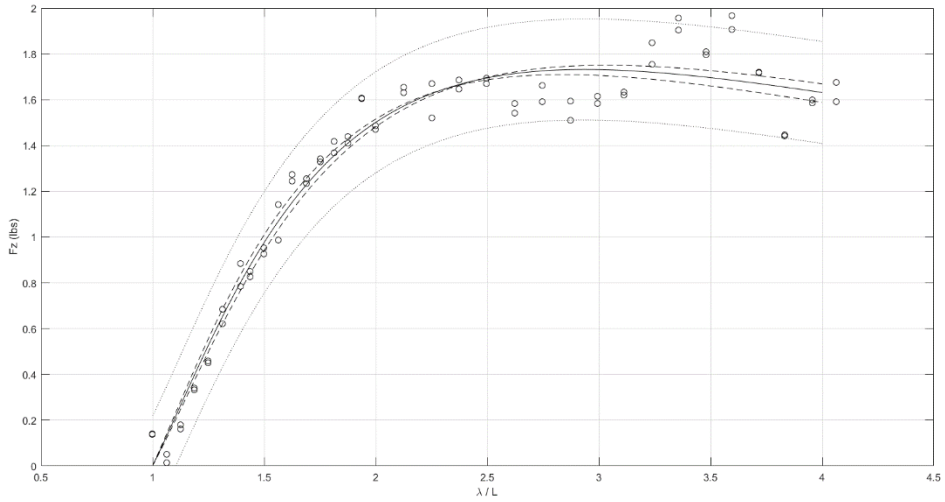

Figure 68. Vertical force results for model with flat face end caps at nondimensional depth of 1.0 at 0.381 m/sec (1.25 ft./sec)

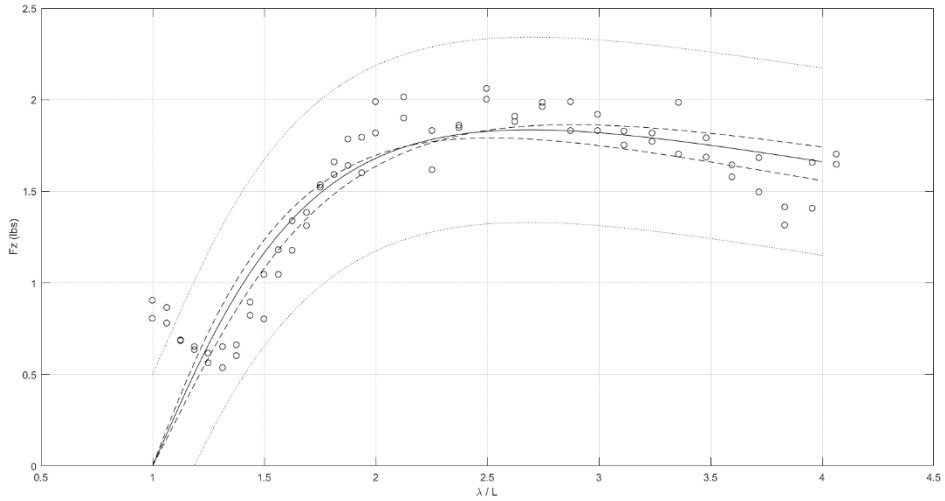

Figure 69. Vertical force results for model with flat face end caps at nondimensional depth of 1.0 at 0.762 m/sec (2.5 ft./sec)

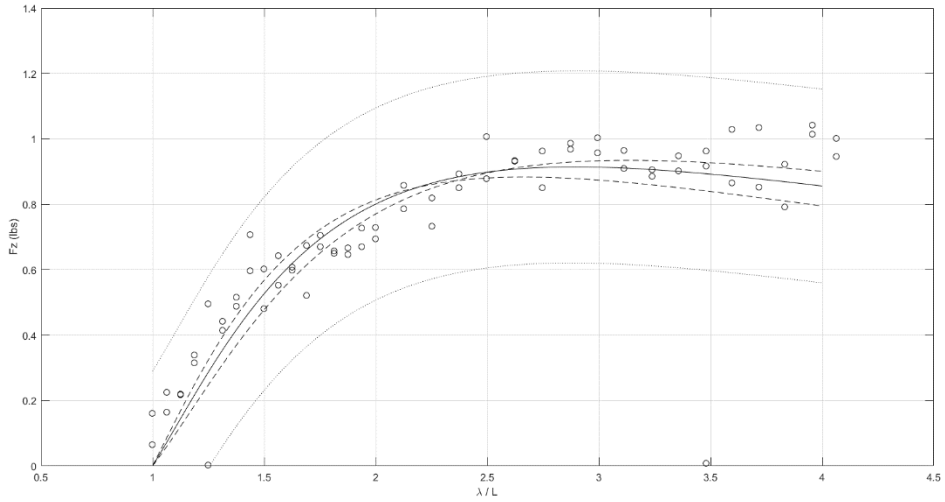

Figure 70. Vertical force results for model with flat face end caps at nondimensional depth of 1.0 at -0.762 m/sec (-2.5 ft./sec)

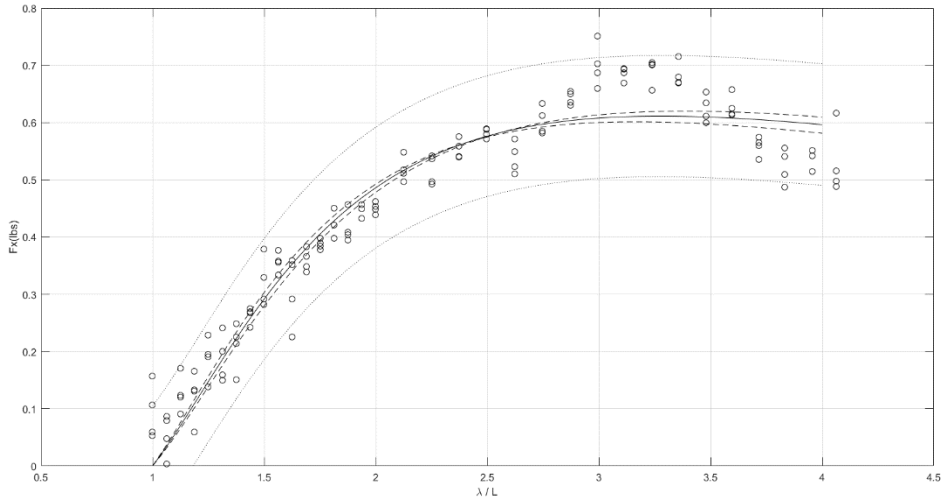

Figure 71. Drag force results for a model with flat face end caps at a nondimensional depth of 2.0 at zero speed

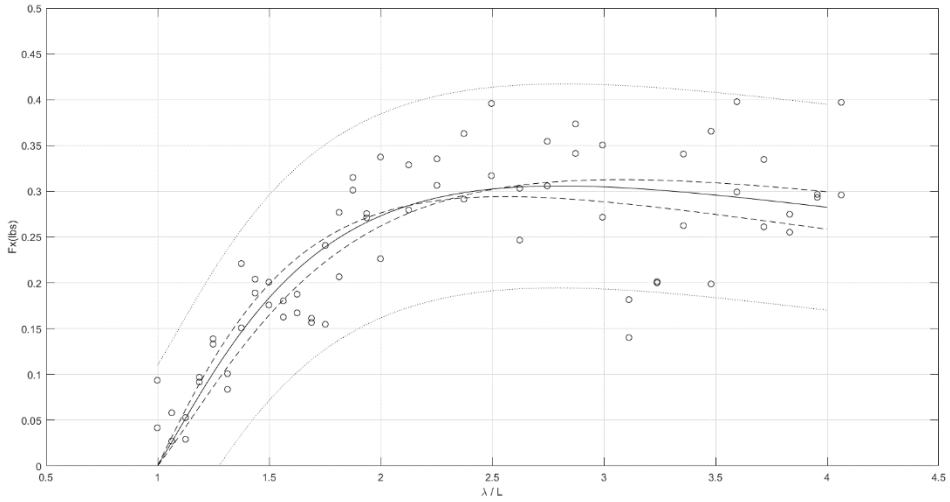

Figure 72. Drag force results for a model with flat face end caps at a nondimensional depth of 2.0 at 0.381 m/sec (1.25 ft./sec)

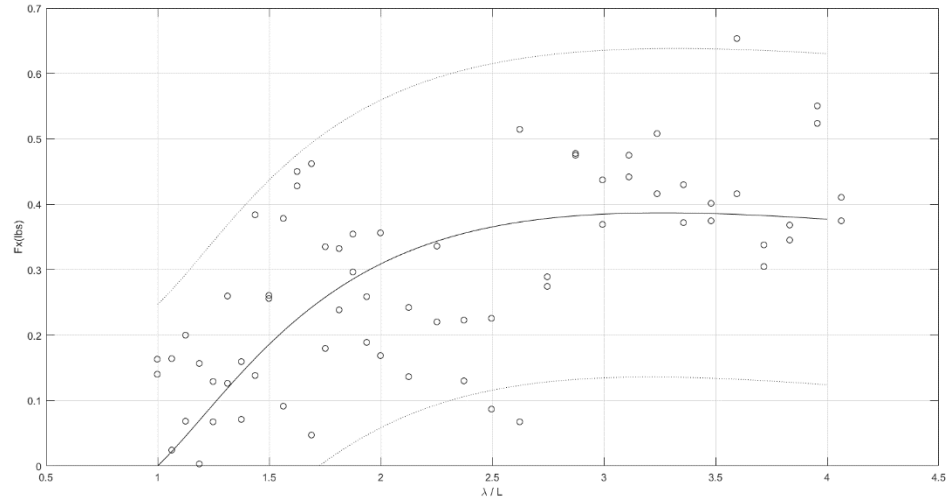

Figure 73. Drag force results for a model with flat face end caps at a nondimensional depth of 2.0 at 0.762 m/sec (2.5 ft./sec)

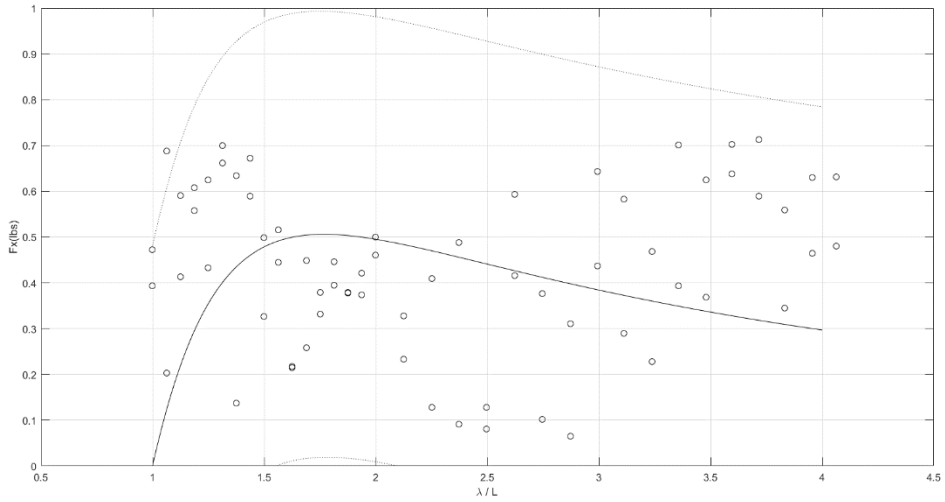

Figure 74. Drag force results for a model with flat face end caps at a nondimensional depth of 2.0 at 0.762 m/sec (2.5 ft./sec)

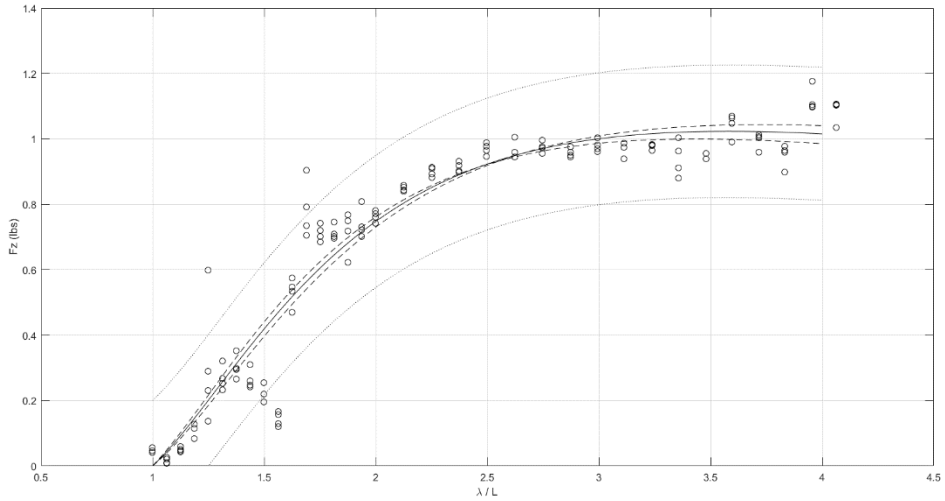

Figure 75. Vertical force results for a model with flat face end caps at a nondimensional depth of 2.0 at zero speed

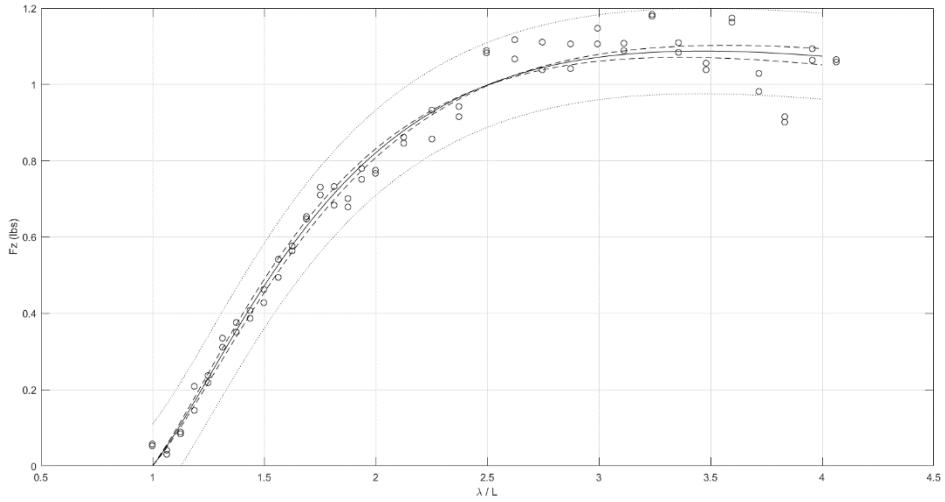

Figure 76. Vertical force results for a model with flat face end caps at a nondimensional depth of 2.0 at 0.381 m/sec (1.25 ft./sec)

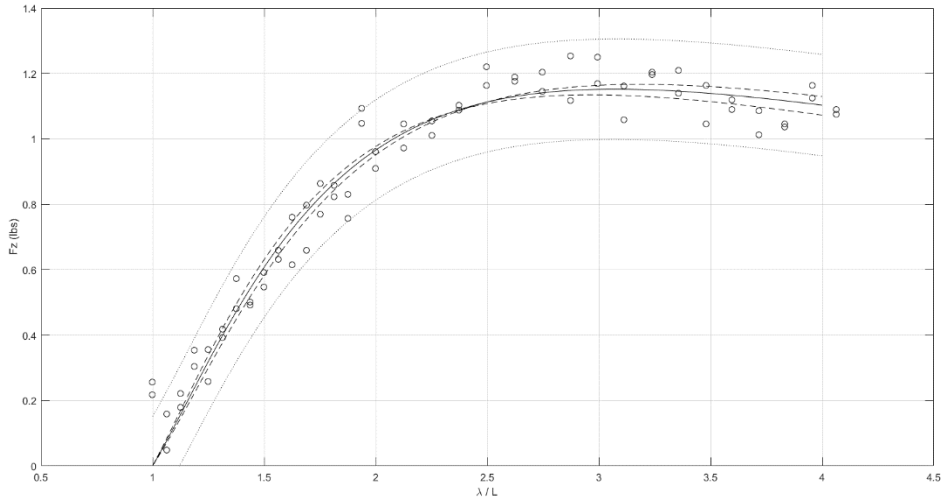

Figure 77. Vertical force results for a model with flat face end caps at a nondimensional depth of 2.0 at 0.762 m/sec (2.5 ft./sec)

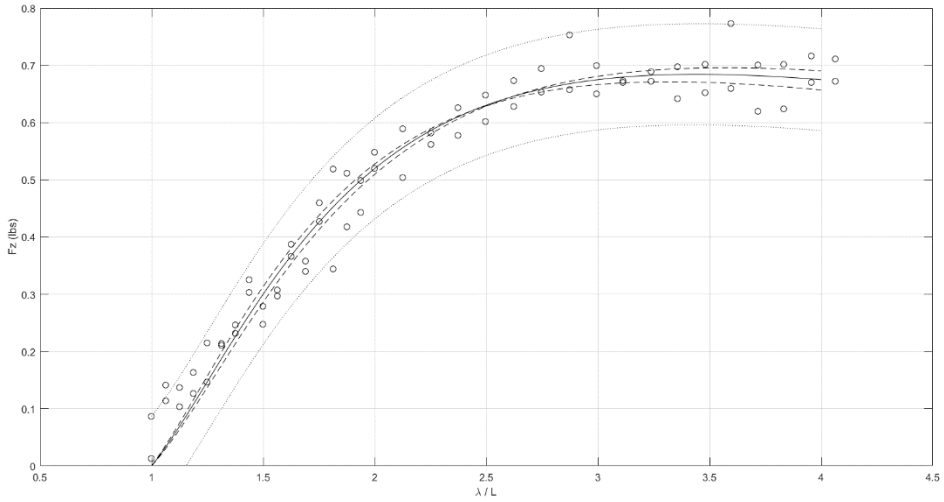

Figure 78. Vertical force results for a model with flat face end caps at a nondimensional depth of 2.0 at -0.762 m/sec (-2.5 ft./sec)

THIS PAGE INTENTIONALLY LEFT BLANK

APPENDIX C. STING DATA RESULTS

The data reduction process that was described in Section III.A explained how the sting-only data was going to be applied to the as-measured combined loads to reveal the hydrodynamic forces experienced on only the model. However, results from the sting-only data showed increasing scatter with increasing velocity. This had been consistently observed throughout the study. Attempting this approach on test cases with forward velocity essentially took data containing substantial noise and used the sting-data, also observed to have substantial noise, to correct it. This introduced more uncertainty into the method and was determined to not always be the best approach in data reduction. Figure 79 shows the as-measured pitch moment for a nondimensional depth of 1.0 and compares it to the pitch moment after using the sting-only data for correction. The sting-only data does not appear to improve the quality for at-speed cases. There is more scatter observed for the longer wavelengths, and with the exception for zero speed cases, the data points shift further away from the theoretical predictions. Zero velocity appears to be the most ideal case to use the sting-only data for pitch moment corrections.

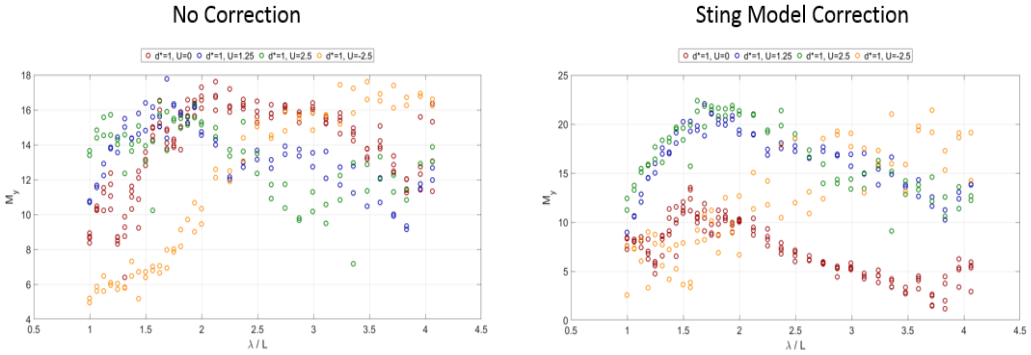

Figure 79. Pitch moment for model with hemispheric end cap at nondimensional depth of 1.0 with no correction compared to pitch moment with sting data correction

The scatter in the sting-only measured drag force was acceptable, so drag force was corrected using the process described in Section III.A. The sting-only measured vertical

force was negligible and was virtually zero so no sting correction was applied to the total vertical force. Due to the amount of scatter in the sting-only measured pitch moment data, an instantaneous drag correction for data reduction was used instead to determine the pitch moment on the model. Figure 80 compares the corrected pitch moment data using the instantaneous drag correction approach to the correction using the sting-only data. The instantaneous drag correction shifts the pitch moment trends down and makes it more agreeable to the theoretical results. The sting-only data correction appears to noticeably increase the amount of scatter in the negative speed case.

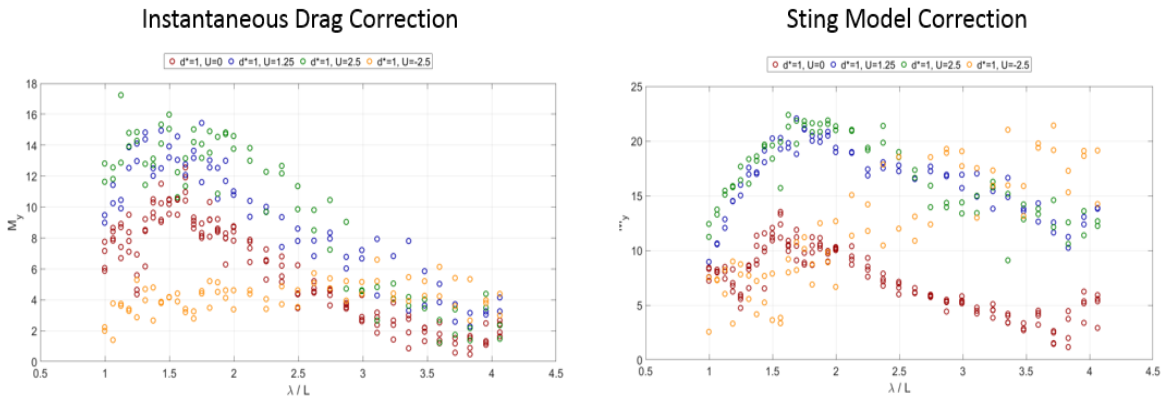

Figure 80. Pitch moment for model with hemispheric end cap at nondimensional depth of 1.0 using the instantaneous drag correction compared to sting data correction

The instantaneous drag correction assumes that the as-measured drag force with the model rigged is equal to the sting-only drag force plus the model-only drag force. Equation 11 is used in the instantaneous drag correction to find the wave-induced pitch moment on the model, $M_{y,M,AH}(t)$. Here, $F_{x,L}(t)$ is the as-measured drag force of the sting and model combined. The pitch moment is corrected by taking the pitch moment induced from the as-measured drag force with the model rigged and the difference in vertical position between the model origin and load-cell, ℓ, and subtracting it from the as-measured pitch moment, $M_{y,L}(t)$, with the model rigged. In this approach, the scattered sting-only data is not used.

$$M_{y,M,AH}(t) = M_{y,L}(t) - \ell F_{x,L}(t) \tag{11}$$

LIST OF REFERENCES

[1] USNI News, "Navy Creating Continual Improvement Program for UUVs through OPNAV, Fleet, NAVSEA." Accessed May 24, 2019. [Online]. Available: https://news.usni.org/2017/11/16/navy-creating-continual-improvement-program-uuvs-opnav-fleet-navsea

[2] Cummins, W. E. Hydrodynamic forces and moments acting on a slender body of revolution moving under a regular train of waves. Tech. Rep. 910, David Taylor Model Basin, West Bethesda, MD, USA, December 1954.

[3] Khalil, G. M., "Experimental investigation of wave forces on submerged horizontal cylinders," *Indian Journal of Engineering and Materials Sciences,* vol. 8, pp. 59–65, Mar. 27, 2000.

[4] P. Ananthakrishnan and K. Zhang, "AUV motion in a wave field," *OCEANS 1998 Conference Proceedings,* vol.2, pp.1059–1063, 1998.

[5] T. M. Turner, J. T. Klamo, and Y. W. Kwon, "Comparison of Wave-Induced Loads on a Near Surface Slender Body From Inviscid Flow Linear Solution and an Experimental Model Test," in *Proceedings of the 37th International Conference on Ocean, Offshore, and Arctic Engineering,* Volume 7A: Ocean Engineering, , Madrid, Spain, Jun 2018.

[6] L.M. Jones, J.T. Klamo, Y.W. Kwon and J.M. Didoszak, "Numerical and experimental study of wave-induced load effects on a submerged body near the surface," in *Proceedings of the 37th International Conference on Ocean, Offshore, and Arctic Engineering,* vol. 7B: Ocean Engineering, Madrid, Spain, Jun 2018, p. V07BT06A048; 9 pages.

[7] S.H. Bolstad, "Hydrodynamic response of a composite structure in an arctic environment," M.S. thesis, Dept. Mech. Eng., Naval Postgraduate School, Monterey, CA, USA 2015.

[8] L. Jones, "Development of a numerical tow tank with wave generation to supplement experimental efforts," M.S. thesis, Naval Postgraduate School, Monterey, CA, USA, 2017.

[9] VS1SP *AC V/Hz and Sensorless Vector Control*. Fort Smith, AR, USA: Baldors Drives, 2009.

[10] A. R. Whitmer, "Predicting wave-induced loads in complex seaways on shallowly submerged vehicles," M.S. thesis, Dept. Mech. Eng., Naval Postgraduate School, Monterey, USA, 2018.

[11] AMTI Force and Motion, “MC3A-100 Specifications.” Accessed May 24, 2019. [Online]. Available: https://www.amti.biz/index.aspx

[12] *ToughSonic General Purpose Series*. Hinesburg , VT, USA: Senix Corporation, 2016.

INITIAL DISTRIBUTION LIST

1. Defense Technical Information Center
   Ft. Belvoir, Virginia

2. Dudley Knox Library
   Naval Postgraduate School
   Monterey, California